Changes in Clouds and the Tropical Circulation in Global Kilometer-Scale Simulations under Different Warming Patterns

LORENZO TOMASSINI[a]

[a] *Met Office, Exeter, United Kingdom*

(Manuscript received 31 January 2024, in final form 9 September 2024, accepted 9 October 2024)

ABSTRACT: One-year-long global kilometer-scale simulations with prescribed sea surface temperatures are presented that are used to study how clouds, convection, and the tropical circulation change under two different warming patterns. The warming patterns, one of which exhibits La Niña–like characteristics and the other an El Niño–like feature, are added to the historical year 2020 and derived from past observed sea surface temperatures. They contain both signatures of natural variability and climate change. Climate sensitivities distinctly differ depending on the warming pattern, mainly due to diverse changes in low clouds over the eastern tropical Pacific. These changes are connected with alterations in larger-scale circulations. Processes related to the interaction between clouds, convection, and circulation are further examined with a focus on the tropical Pacific. Better understanding those processes helps elucidate apparent discrepancies between recent observed trends over the tropical Pacific and trends simulated by low-resolution global climate models. Evidence suggests an active role of moisture dynamics in shaping low-level moist static energy anomalies over the western tropical Pacific and a positive feedback of resulting moist convection on larger-scale zonal circulations, including over the eastern Pacific subsidence region. Complementary to the global kilometer-scale simulations, the same experiments are conducted with a lower-resolution model version in which convection is parameterized. Even though climate sensitivities and the broad responses are not strongly changed, the differences in the convection-permitting experiments might still be consequential in global coupled climate simulations.

KEYWORDS: Atmospheric circulation; Clouds; Convection; Climate sensitivity

1. Introduction

In various ways, the climate change signal has been emerging from natural variability or reached an amplitude of similar magnitude over recent years. It is often not possible to clearly separate the effects of natural fluctuations from the influence of external forcings based solely on observations. However, a clear separation of climate variability from long-term climate change is not always the appropriate or most pressing question. A better understanding of multiannual or multidecadal changes of the climate system, and the processes involved, can be an equally or even more important objective. Under the given circumstances, these multiannual and multidecadal changes will involve both a climate change signal as well as aspects of natural variability. In the present study, global kilometer-scale simulations are used in a methodology that is similar in spirit to a storyline approach (Shepherd 2019; Ghosh and Shepherd 2023). Possible future climate outcomes are investigated that can involve both natural variability and climate change with a focus on physical processes.

Surface temperature or near-surface temperature is an obvious place to start. Changes in surface temperature are not only important due to their direct effect on ecosystems and livelihoods; it has also been established that climate change feedbacks are mediated mainly through surface temperature changes (e.g., Tomassini et al. 2013; Loeb et al. 2016). Moreover, these feedbacks, and in particular the response of clouds to surface temperature changes, depend on the geographical pattern of the change (Andrews et al. 2015; Stevens et al. 2016; Andrews et al. 2022). Since not only the global-mean temperature but also the pattern of surface temperature change exhibits variability in time, climate change feedbacks such as the cloud or lapse rate feedback also show an evolution in time (Senior and Mitchell 2000; Armour et al. 2013).

The dependence of climate change feedbacks on patterns of surface temperature change has been particularly notable in the region of the tropical Pacific over recent decades (Fueglistaler 2019; Dong et al. 2019; Fueglistaler and Silvers 2021; Ceppi and Fueglistaler 2021; Watanabe et al. 2023). Especially over the tropical Pacific, but also in other parts of the world, the developing warming pattern is likely related to the coupling between convection and the atmospheric circulation in one way or another (Back and Bretherton 2005; DiNezio et al. 2009; England et al. 2014; Tomassini et al. 2015; Tomassini 2020). Thus, the question of how surface warming patterns evolve over time is related to how the tropical circulation, the structure of the tropical atmosphere, and tropical convection alter and interact with each other (Hartmann et al. 2022). The interaction between convection and the tropical circulation under warming is an intricate and multifaceted question, and some advances in understanding the problem have been made mainly based on idealized studies (Jenney et al. 2020; Jeevanjee 2022). However, idealized model experiments often make simplifying assumptions such as atmospheric convection being in some form of equilibrium with its environment. These assumptions are not always accurately

Denotes content that is immediately available upon publication as open access.

Corresponding author: Lorenzo Tomassini, lorenzo.tomassini@metoffice.gov.uk

DOI: 10.1175/JCLI-D-24-0068.1

fulfilled in the real world, especially on shorter time scales of hours to days or in the situation of a transient, evolving climate.

Related to observed changes in surface temperature, it has been suggested that low-resolution global climate models struggle to reproduce the observed warming pattern over the tropical Pacific in recent decades, in particular after 1980 and up to the year 2014, even when taking natural variability into account (Cane et al. 1997; Seager et al. 2019, 2022; Wills et al. 2022). Recent sea surface temperature (SST) trends in the tropical Pacific have exhibited a more La Niña–like feature, while low-resolution coupled climate models project longer-term warming patterns that resemble El Niño–like conditions. A key process that is not resolved in low-resolution climate models and has to be parameterized in the form of a simple one-dimensional column model is atmospheric convection. The issue with parameterizing convection is not only the simplified representation of the process but also the way in which convection is coupled to the larger-scale atmospheric dynamics in such low-resolution models. Convection-permitting simulations which partially resolve convection, in contrast, can produce different atmospheric profiles (Holloway et al. 2012) and, in principle, couple differently to larger-scale temperature gradients and atmospheric circulations in the tropics (Tomassini 2020).

In the present study, we use a global convection-permitting atmospheric model which partially resolves convection and compare it to lower-resolution simulations with parameterized convection. The model is run for the historical year 2020 using prescribed daily varying SSTs. Two additional 1-yr-long simulations are performed each with a different sea surface temperature pattern added to the time-varying SSTs of the year 2020. The two warming patterns are chosen in such a way that one exhibits more "La Niña–like" characteristics and the other exhibits a more "El Niño–like" feature. Our work complements other studies which have prescribed a uniform warming pattern on top of the historical year (Cheng et al. 2022; Bolot et al. 2023).

The atmosphere-only simulations cannot explain how and why the historical sea surface temperature warming patterns developed over the tropical Pacific. However, a better understanding of how clouds, convection, and the tropical circulation interact and respond to different warming patterns can give insights into feedbacks which are likely to be important in the processes that influence the warming patterns.

The article is structured as follows. Section 2 describes the numerical experiments and the model configurations that are used. The model configurations include a convection-permitting 5-km resolution model and a 25-km resolution setup with parameterized convection. In section 3, the climate sensitivities of the different model configurations under different warming patterns are estimated, and the connection of climate sensitivity with cloud and circulation changes is explored. To better understand the connection between clouds and the characteristics of the atmospheric circulation in the tropics, the response of the distributions of vertical motion and their relationships to clouds is first examined for the tropics as a whole in section 4. Section 5 then zooms into the tropical Pacific, a region of global importance when it comes to climate change, and investigates the link between the larger-scale atmospheric circulation, rainfall, and clouds, both in the historical 2020 experiments on time scales of days and in the different warming experiments analyzing changes in yearly mean characteristics. A section with a summary and discussion concludes the article.

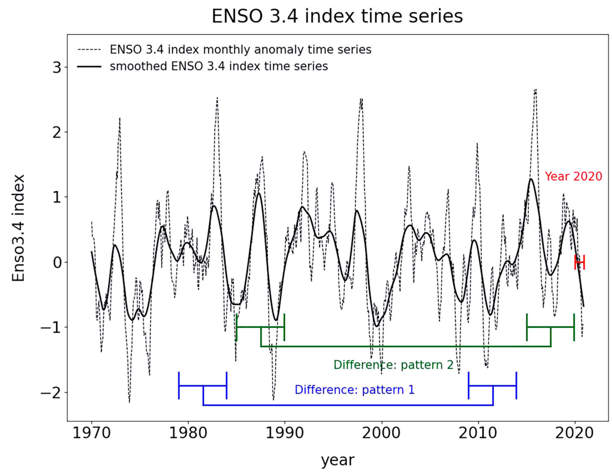

FIG. 1. El Niño Southern Ocean 3.4 index based on the HadISST dataset (Rayner et al. 2003). The figure illustrates the motivation for the definition of the two warming patterns. The first pattern is defined as the difference between the mean over the years 2009–13 and the mean over the years 1979–83; this difference results in a La Niña–like anomaly. The second pattern is defined as the difference between the mean over the years 2015–19 and the mean over the years 1985–89; this difference results in an El Niño–like anomaly. A 30-year period lies between the two averaging intervals that define the respective patterns. The smoothing of the ENSO-3.4 time series uses a locally weighted linear regression with 5% of the data used when estimating each y value.

2. Model experiments and configurations

For the present study, three 1-yr-long global 5-km resolution simulations were performed using the Met Office Unified Model in a convection-permitting configuration. In the first experiment, the historical year 2020 is simulated with prescribed, daily varying SSTs using Operational SST and Ice Analysis (OSTIA). In the two other yearlong simulations, two different constant warming patterns are added to the historical SSTs of the year 2020, and the resulting daily varying SSTs are used to force the global atmospheric model. In addition, the same three 1-yr-long simulations were also conducted with a 25-km resolution model configuration in which convection is parameterized.

The warming patterns are constructed by averaging ERA5 (Hersbach et al. 2020) SSTs over two 5-yr-long historical periods and subtracting them from each other. The first warming pattern (pattern 1) is the mean over the years 2009–13 minus the mean over the years 1979–83; the second pattern (pattern 2) is the mean over the years 2015–19 minus the mean over the years 1985–89. The averaging periods are indicated in Fig. 1. The main motivation for choosing the different periods is related to El Niño–Southern Oscillation (ENSO) variability in the tropical Pacific. Pattern 1 is constructed in such a way that it exhibits a

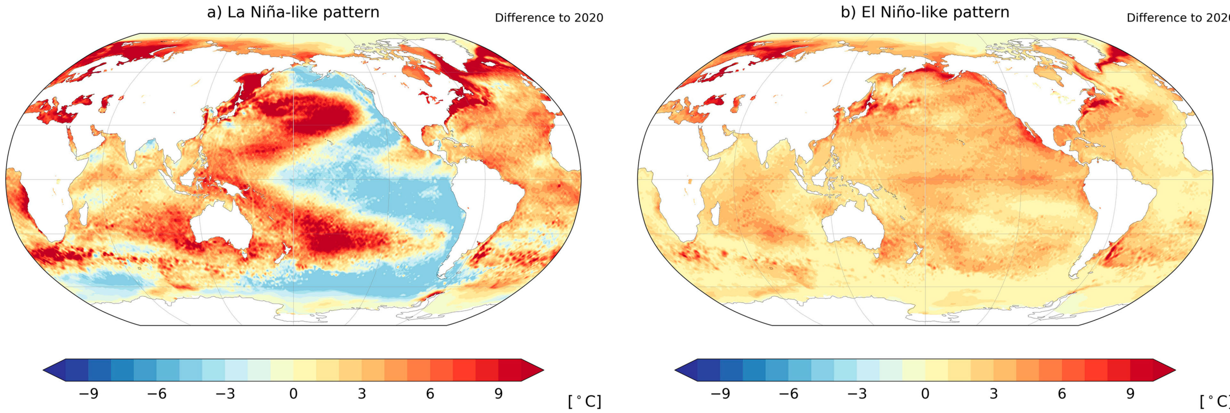

FIG. 2. The two SST patterns that are added to the daily varying SSTs of the year 2020 for the warming pattern experiments. (a) La Niña–like warming pattern. (b) El Niño–like warming pattern. Here, the patterns are shown at 25-km resolution.

pattern strongly influenced by a La Niña phase in the tropical Pacific, and pattern 2 is defined in such a way that it exhibits a pattern strongly affected by an El Niño phase. For ease of reading, we call pattern 1 the La Niña–like pattern and pattern 2 the El Niño–like pattern in the following (Fig. 2). The two patterns are warming patterns in the sense that for each pattern, there is a 30-yr period in between the two 5-yr averaging intervals, and therefore, a global-mean temperature warming is implicit in the two patterns apart from the respective signature of natural variability. The difference between the two patterns that is most relevant in the context of the present study is related to the warming signal over the tropical Pacific: in the La Niña–like pattern, the western Pacific deep convective region warms significantly, whereas the eastern Pacific subsidence area cools, and in the El Niño–like pattern, the warming extends across the whole of the Pacific with more pronounced warming in the eastern and central equatorial Pacific compared to the western part of the basin.

To be able to identify distinct signals in the warming simulations, the two patterns are scaled: the La Niña–like pattern is scaled by a factor of 10 and the El Niño–like pattern is scaled by a factor of 5.2. The scaling factors were chosen in such a way that the global-mean SST warming is about the same for both patterns and lies between 3° and 4°C. Due to the different degrees of land warming in the two simulations, the global yearly mean temperature change is 3.9°C in the La Niña–like warming pattern simulation and 3.1°C in the El Niño–like warming pattern simulation; the tropical-mean warming is very similar in magnitude in both patterns, though. All simulations are initialized from ERA5 initial conditions. The historical year 2020 simulation is started on 1 January 2020. The warming simulations are started on 1 December 2019; from there, the warming patterns are ramped up linearly over the course of December 2019 in such a way that they attain their scaled value on 31 December 2019. The ramping up of the warming patterns over the course of 1 month allows for a certain degree of adjustment of quantities such as soil moisture.

The sea ice cover in the warming simulations is adopted from the daily varying year 2020 sea ice. When adding the warming patterns to the SSTs of the year 2020, two conditions are observed. The SST is not changed when and where there is sea ice. Moreover, the 10% and 90% quantiles over all grid points are computed for the two warming patterns based on all grid points of the ERA5 skin temperature, including land points. The two quantiles are then used to cap the SST patterns (before scaling) prescribed in the warming simulations. The latter condition is introduced in order to avoid very extreme local SST changes after scaling the patterns. Figure 3 (top row) shows the warming patterns in ERA5, including land points, and the warming patterns based on the yearly mean surface temperature change between the warming simulations and the historical year 2020 simulation at 5-km resolution (bottom row). It is interesting to note that the land temperature changes are somewhat different in ERA5 compared to the corresponding 5-km resolution model simulations, an issue that is not further investigated here. The yearly mean surface temperature changes are quite similar in the 25-km resolution simulations as they are in the 5-km resolution simulations (not shown). The differences to ERA5 could be caused by biases in the land surface scheme, limited spinup of land surface processes, a nonlinear response of land temperatures to the scaling of the prescribed SST patterns, or the fact that aerosols are not changed in the warming experiments.

As mentioned in the introduction, the imprint of ENSO variability in the warming patterns is of interest because longer-term, multidecadal warming signals can show features similar to ENSO-related anomalies in the tropical Pacific. For instance, the observed near-surface temperature trend over the years 1991–2020 (Fig. 4) exhibits a La Niña–like structure over the tropical Pacific. The linear trends computed from three different observational datasets, NOAA GlobalTemp version 5 (Zhang et al. 2023), HadCRUT5 (Morice et al. 2021), and ERA5 (Fig. 4), have similar spatial features with equal or more pronounced warming in the western tropical Pacific deep convective areas compared to the eastern Pacific subsidence regions. The long-term warming patterns of global coupled climate models, on the other hand, typically show El Niño–like characteristics with more distinct warming in the equatorial eastern Pacific (DiNezio et al. 2009). Linear warming trends over the model years 1984–2014 from arbitrarily selected realizations of the historical simulations in four coupled global climate models

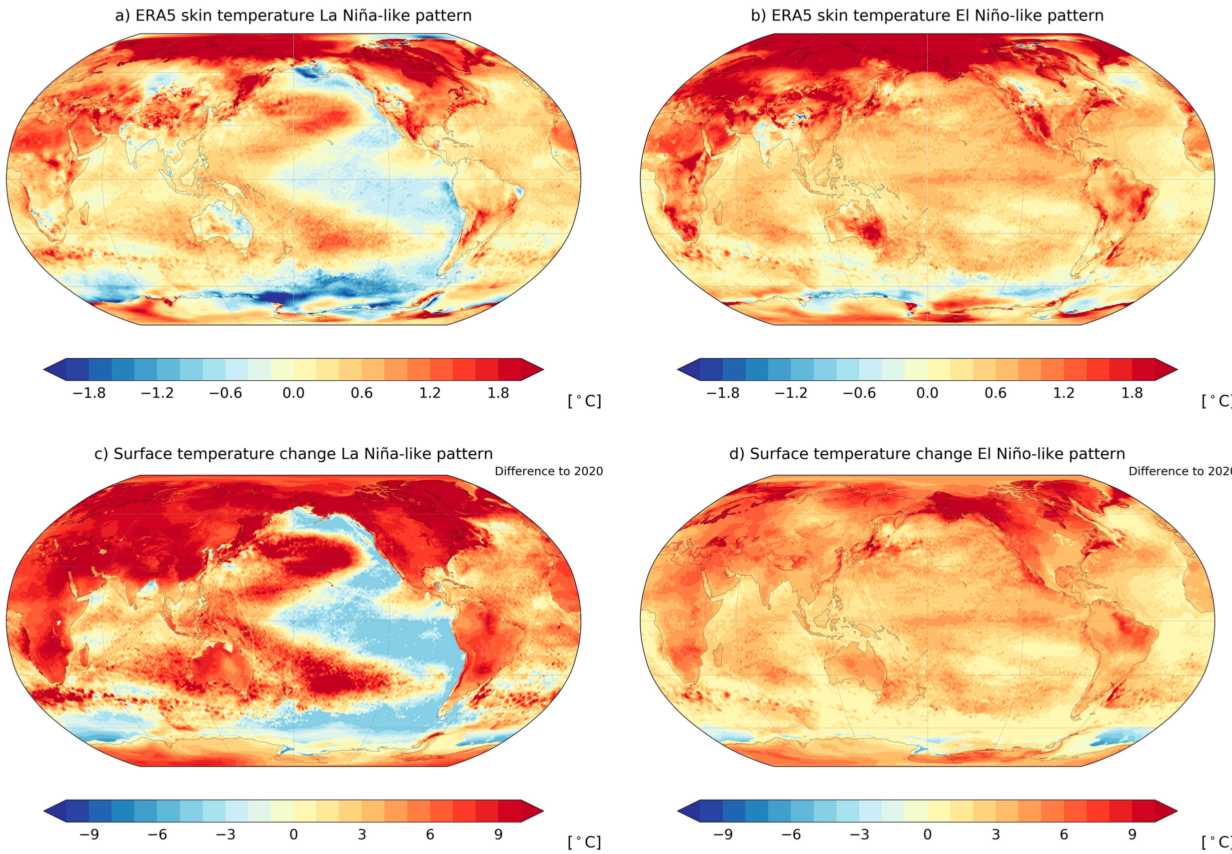

FIG. 3. (top) The two unscaled patterns as derived from ERA5 skin temperature, including land temperatures. (bottom) Difference between the yearly mean surface temperature of the respective warming pattern experiment and the historical 2020 simulation based on the 5-km resolution model experiments.

(Fig. 5) show a mixture of aspects, but the gradient of the warming trend in the tropical equatorial Pacific from the western Maritime Continent to the eastern subsidence region off the coasts of Ecuador and Peru typically exhibits the opposite sign compared to the observational datasets. In the historical simulations shown in Fig. 5, the difference between models and observations may not be particularly obvious, except for the Met Office Hadley Centre (MOHC) model. A discussion of the multimodel mean trend over a similar time period can be found in Seager et al. (2022). For statistical analyses of the discrepancy between models and observations, often a relatively restricted latitude band around the equator is considered such as 10°S–10°N, or narrower (Seager et al. 2022).

We turn to the description of the global model configurations used in the present study. For the 5-km resolution convection-permitting simulations, the configuration *MidLevShConv25RAturb* is employed as described in Tomassini et al. (2023) with two minor modifications which are designed to make the model more stable, particularly in polar regions. The fraction of maximum diffusion in

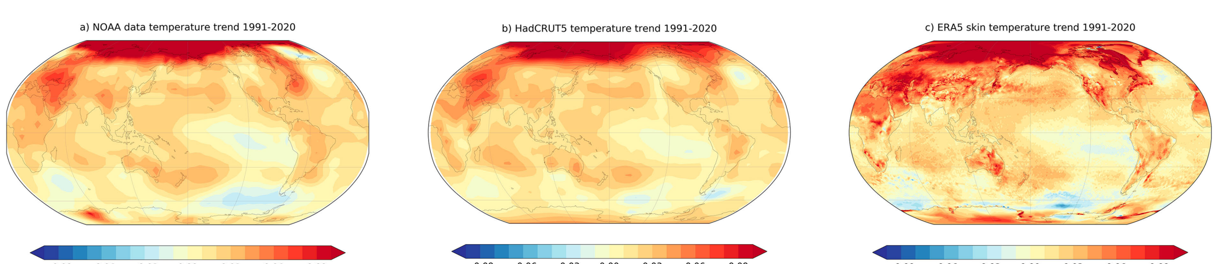

FIG. 4. Observed surface or near-surface temperature linear trends over the period 1991–2020 based on different observational products. (a) NOAA GlobalTemp version 5 dataset (Zhang et al. 2023), (b) HadCRUT5 dataset (Morice et al. 2021), and (c) ERA5 skin temperature.

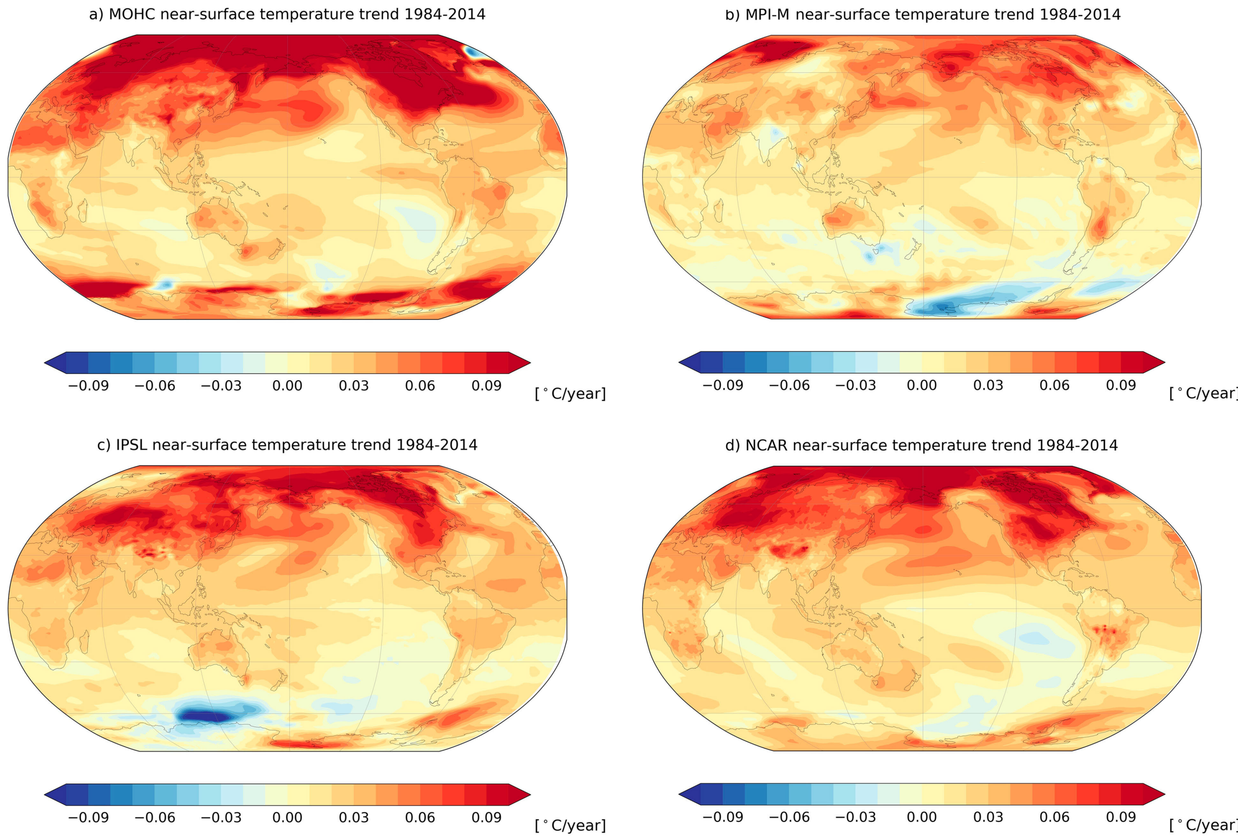

FIG. 5. Near-surface temperature linear trends over the period 1984–2014 from four models of the phase 6 of the Coupled Model Intercomparison Project (CMIP6) based on an arbitrarily chosen realization of the coupled historical simulation. (a) MOHC model (HadGEM3-GC31-LL), (b) Max Planck Institute for Meteorology (MPI-M) model (MPI-ESM1-2-LR), (c) L'Institut Pierre-Simon Laplace Coupled Model, version 6A, low resolution (IPSL-CM6A-LR), and (d) National Center for Atmospheric Research (NCAR) model (CESM2).

the boundary layer blending scheme (Boutle et al. 2014) is decreased from 0.75 to 0.5, and the parameter in the nonlinearity setting for the boundary layer solver in the case of stable boundary layers is increased from 2 to 4. Both changes help minimize model failures in or near the top of the boundary layer at high latitudes. In all the simulations, there were only two model failures, namely, in the La Niña–like warming simulation. Both model failures could be circumvented by reducing the model time step from 90s to 60s for the duration of the particular model day on which the failure occurred. The configuration *MidLevShConv25RAturb* is a convection-permitting configuration with a reduced mass-flux convection scheme; in Tomassini et al. (2023), it was estimated that about 30% of the rainfall is produced by the convection parameterization and 70% of the rainfall is produced by the large-scale microphysics scheme. The 25-km resolution simulations are based on the configuration *GA7.0* (Walters et al. 2019) for which convection is mostly parameterized. The global model configuration *GA7.0* was also used as a reference in Tomassini et al. (2023). One should note that the shallow convective mass flux is reduced only modestly in *MidLevShConv25RAturb,* and therefore, the parameterization of shallow convection does not differ strongly between the configurations *GA7.0* and *MidLevShConv25RAturb*. However, the treatment of turbulence in the boundary layer and the convective mass flux out of the boundary layer related to deeper clouds is represented substantially differently.

The top-of-the-atmosphere (TOA) radiative fluxes in the historical year 2020 simulations are close to being balanced and in quite good agreement with observational estimates. For the 5-km resolution simulation, the global-mean net radiative flux imbalance averaged over the whole year is −0.47 W with 240.40 W m^{-2} for the global-mean outgoing longwave radiative flux and 100.49 W m^{-2} for outgoing shortwave radiative flux. The same quantities for the 25-km resolution simulation are −0.2 W m^{-2} TOA net radiative flux imbalance with 242.05 W m^{-2} for the global-mean outgoing longwave radiative flux and 98.57 W m^{-2} for the outgoing shortwave radiative flux. Dübal and Vahrenholt (2021) give observational estimates for the year 2020 TOA outgoing longwave radiative flux of 240.9 and for the outgoing shortwave radiative flux of 98.3 W m^{-2}.

3. Climate sensitivity and cloud response

As already discussed in the introduction, previous work suggests that the sensitivity of the climate system to warming depends on the pattern of warming. This question merits

TABLE 1. Changes in TOA radiative fluxes, the global-mean temperature, and climate sensitivity estimates for the two warming patterns at 5- and 25-km resolution. The first column indicates the experiment. The second column includes the yearly mean difference in TOA OLR between the warming pattern experiment and the historical 2020 simulation. The third column includes the yearly mean difference in TOA OSR between the warming pattern experiment and the historical 2020 simulation. The fourth column contains the yearly mean difference in net TOA radiative flux between the warming pattern experiment and the historical 2020 simulation. The fifth column gives the global-mean temperature change. The sixth column shows the climate sensitivity estimate based on the respective experiment.

Warming experiment	ΔTOA OLR ($W\ m^{-2}$)	ΔTOA OSR ($W\ m^{-2}$)	ΔTOA net radiative flux ($W\ m^{-2}$)	ΔT (K)	Climate sensitivity (K)
5-km La Niña–like pattern	12.57	−2.17	10.4	3.90	1.39
25-km La Niña–like pattern	14.14	−3.96	10.18	3.97	1.45
5-km El Niño–like pattern	8.09	−4.81	3.28	3.08	3.48
25-km El Niño–like pattern	9.09	−5.75	3.34	3.18	3.53

further attention to better understand the processes involved, in particular the role of convection and convection–circulation coupling. Moreover, a priori, it is not inconceivable that the convection-permitting global model responds very differently to global warming or particular warming patterns than a parameterized convection model. In the present section, we therefore first estimate climate sensitivity from the different warming simulations and then investigate the main causes of the differing model behaviors.

a. Climate sensitivity estimates

In the atmosphere-only simulations in question, the CO_2 concentration is not changed; the warming is imposed by prescribing the SSTs. There is a way of roughly estimating equilibrium climate sensitivity, the equilibrium global-mean temperature change after a doubling of the CO_2 concentration in the atmosphere, based on such simulations. The estimate is an approximation, and it does not include all the processes. For example, the direct effect of the CO_2 concentration change on atmospheric temperatures and changes in sea ice under warming are not included. Nevertheless, the experience with lower-resolution simulations suggests that the approximation gives a qualitatively useful result, especially in a relative sense when simulations and model versions are compared with each other (Senior and Mitchell 2000; Tomassini et al. 2013; Andrews et al. 2018; Bodas-Salcedo et al. 2019).

To estimate climate sensitivity, taking into account that the CO_2 concentration is not changed in the different simulations, the following formula is used:

$$\text{climate sensitivity} = \frac{\Delta T}{\Delta G} \times 3.71\ \mathrm{W\,m^{-2}},$$

where ΔT is the global-mean surface temperature change between the historical and the warming simulation, ΔG is the net TOA radiative flux difference between the historical and the warming simulation, and 3.71 $W\ m^{-2}$ is the assumed external forcing corresponding to a doubling of the CO_2 concentration (Myhre et al. 1998). The idea here is to consider the net TOA radiative flux difference between the historical and the warming simulation as the forcing that is needed to attain the (essentially prescribed, apart from the land temperatures) surface temperature change. In addition, it is of interest to consider not only the changes in the TOA net radiative flux but also the shortwave and longwave radiative flux changes individually because they give some indications about the processes involved. Table 1 summarizes the result of the analysis.

b. Outgoing longwave radiative fluxes and high cloud cover

Differences in outgoing longwave radiation (OLR) are expected to scale approximately linearly in global-mean surface temperature (Richards et al. 2021). Indeed, the differences in OLR between the La Niña–like warming pattern simulations and the El Niño–like warming pattern simulations are largely explained by the differences in global-mean surface temperature change when assuming a linear relationship. This holds more so for the 5-km resolution simulations than the 25-km resolution simulations, a point that will be discussed further below. The remaining differences in OLR changes between the two patterns are also partly due to differing changes in relative humidity (Allan et al. 1999). Because the stronger drying in the La Niña–like warming pattern simulations occurs mainly in relatively moist parts of the tropics, the impact on OLR changes is limited, however (Fig. 6). Moreover, changes in OLR due to clouds occur mainly in deep convective regions where the OLR changes are largely offset by opposite changes in outgoing shortwave radiation (L'Ecuyer et al. 2019) and therefore do not have a strong impact on climate sensitivity (see Fig. 10 for the La Niña–like warming pattern).

Outgoing longwave radiative fluxes are affected by high clouds because high clouds have low cloud-top temperatures and therefore typically exhibit small thermal emission compared to the cloud-free surface (Luo et al. 2023). The difference in changes in global-mean high cloud cover between the two warming patterns is modest (Fig. 7). Here, high cloud cover is defined to include clouds between 500 and 150 hPa using a maximum overlap assumption (Tompkins and Di Giuseppe 2015). In the 5-km resolution La Niña–like warming simulation, the global-mean high cloud cover decreases by 3.8%, and in the 5-km resolution El Niño–like warming simulation, it decreases by 1.8%. There are, however, differences in terms of the patterns of change, as to be expected.

In the La Niña–like warming simulation, there is a marked increase of high clouds over the Maritime Continent and along two strong low-level convergence zones in the western

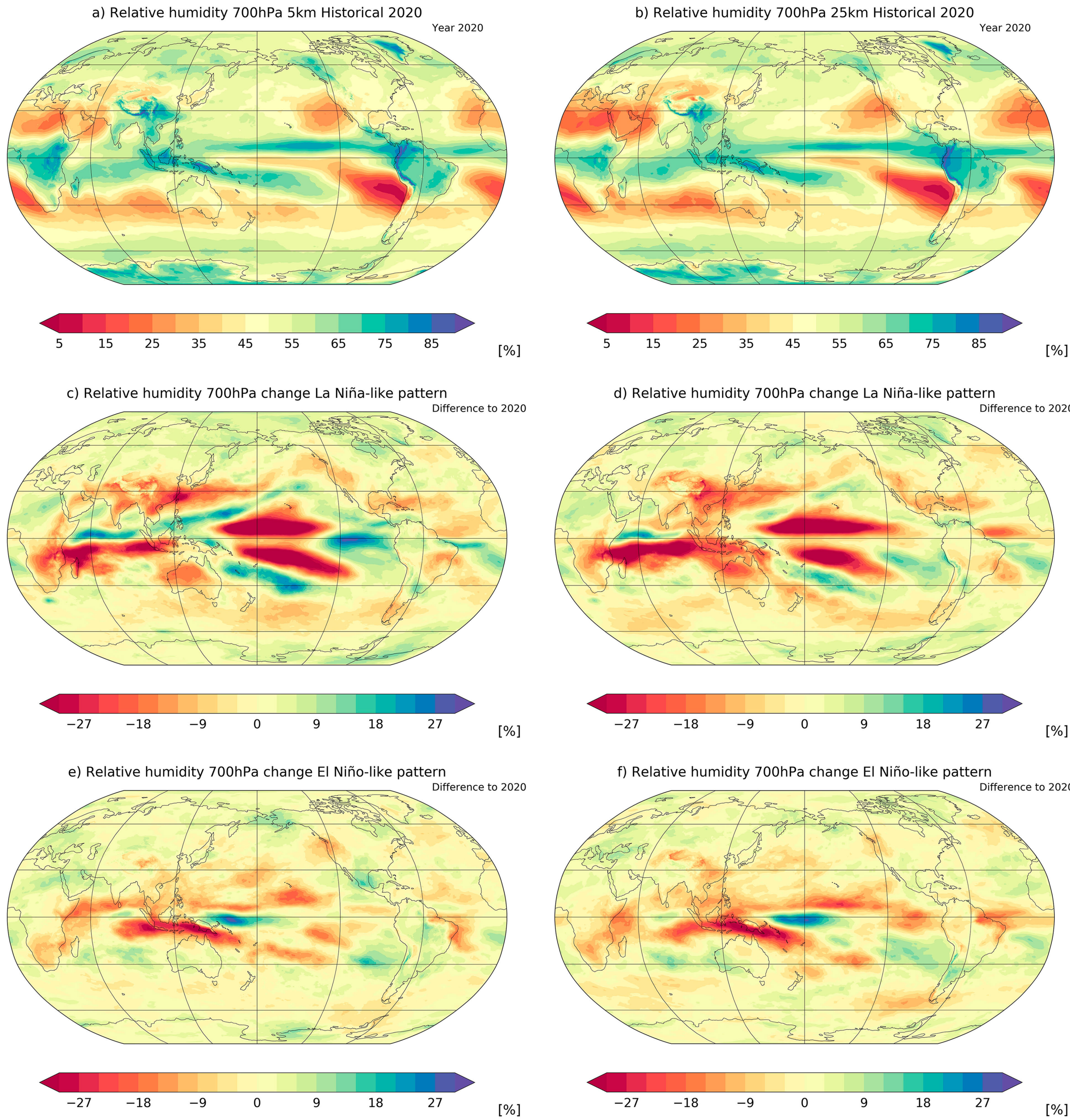

FIG. 6. (a) Yearly mean relative humidity at 700 hPa in the 5-km resolution historical 2020 simulation. (b) Yearly mean relative humidity at 700 hPa in the 25-km resolution historical 2020 simulation. Changes in yearly mean relative humidity at 700 hPa for the La Niña–like warming pattern simulations at (c) 5-km resolution and (d) 25-km resolution. Changes in yearly mean relative humidity at 700 hPa for the El Niño–like warming pattern simulations at (e) 5-km resolution and (f) 25-km resolution.

tropical Pacific: one oriented toward the northeast in the Northern Hemisphere and one oriented toward the southeast in the Southern Hemisphere. To some extent, the two branches are seasonal features, but they are both present to varying degrees throughout the year and related to the time-invariant warming pattern. Conversely, in many other parts of the tropics, the intertropical convergence zone (ITCZ) weakens. In particular, the ITCZ north of the equator over the eastern Pacific vanishes almost completely (see also the second row of Fig. 12 for the pressure velocity at 500 hPa). In contrast, in the El Niño–like warming simulation, this part of the ITCZ over the eastern Pacific becomes more pronounced, and high cloud cover over the Maritime Continent in the western Pacific is strongly diminished or shifts to the east to some extent. Interestingly, some other changes are quite robust across the two warming patterns, like the decrease in high cloud cover over the Congo basin in

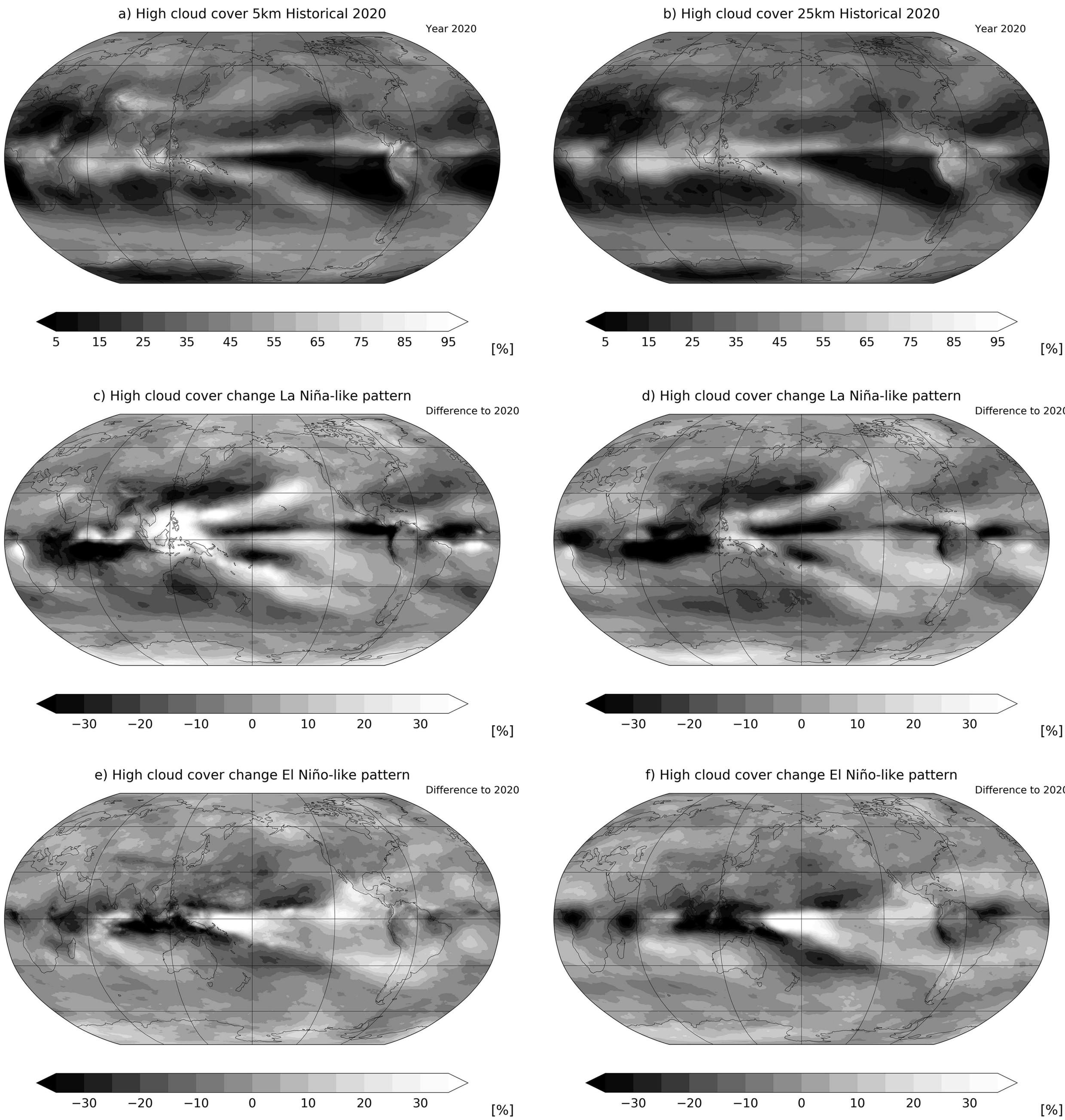

FIG. 7. (a) Yearly mean high-cloud cover in the 5-km resolution historical 2020 simulation. (b) Yearly mean high-cloud cover in the 25-km resolution historical 2020 simulation. Changes in yearly mean high cloud cover for the La Niña–like warming pattern simulations at (c) 5-km resolution and (d) 25-km resolution. Changes in yearly mean high-cloud cover for the El Niño–like warming pattern simulations at (e) 5-km resolution and (f) 25-km resolution.

Africa, the oceanic ITCZ over the tropical Atlantic, and the ITCZ over the western and eastern Indian Ocean. With regard to these features, the lower-resolution simulations with parameterized convection show a more consistent behavior across the warming patterns than the 5-km resolution convection-permitting simulations (Figs. 7d and 7f compared to Figs. 7c and 7e). The changes in high cloud cover closely mirror the changes in the tropical rainbands and the divergence at 850 hPa (not shown). The divergence at 850 hPa generally agrees well with the position of the rainbands in the tropics (Lindzen and Nigam 1987; Back and Bretherton 2009; Tomassini 2020).

c. *Outgoing shortwave radiative fluxes and low cloud cover*

Low clouds do not have a strong influence on OLR because the cloud-top temperatures of low clouds are not very

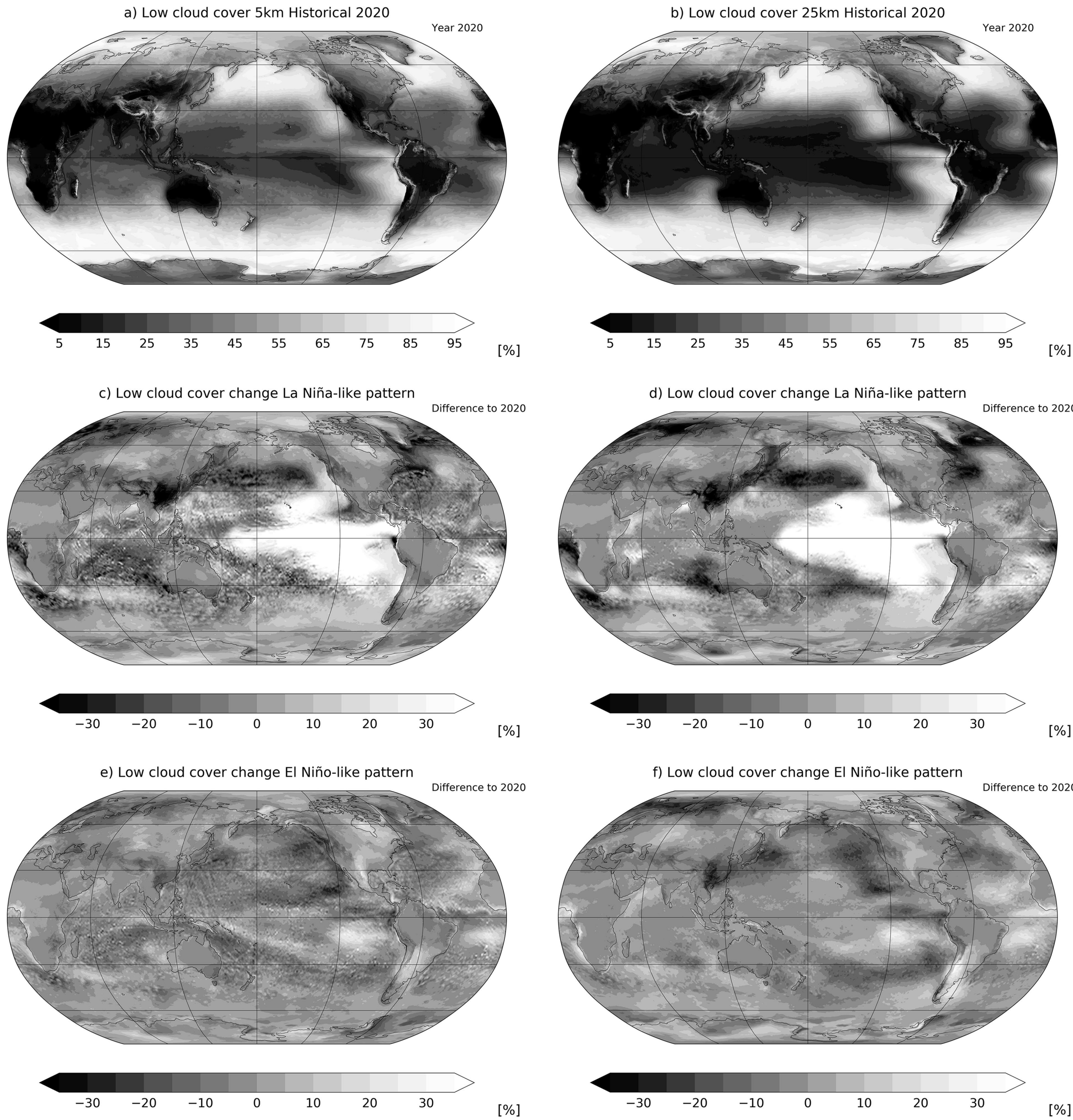

FIG. 8. (a) Yearly mean low-cloud cover in the 5-km resolution historical 2020 simulation. (b) Yearly mean low-cloud cover in the 25-km resolution historical 2020 simulation. Changes in yearly mean low-cloud cover for the La Niña–like warming pattern simulations at (c) 5-km resolution and (d) 25-km resolution. Changes in yearly mean low-cloud cover for the El Niño–like warming pattern simulations at (e) 5-km resolution and (f) 25-km resolution.

different from the surface temperature. Due to their abundance, especially over tropical oceans, they exert a strong influence on the TOA outgoing shortwave radiation (OSR), though (Luo et al. 2023).

From the discussion so far, we can conclude that the difference in climate sensitivity between the two warming patterns is mainly caused by the difference in the change in the outgoing shortwave radiative flux. Given that sea ice is kept fixed, the latter is mainly related to differing changes in low cloud cover (Fig. 8). In the 5-km resolution simulation, the reduction in OSR in the El Niño–like warming simulation is more than double compared to the La Niña–like warming simulation (Table 1). The reason is quite obvious when looking at the yearly mean changes in low cloud cover for the different simulations: in the La Niña–like warming experiment, there is a strong increase in low cloud cover over the central

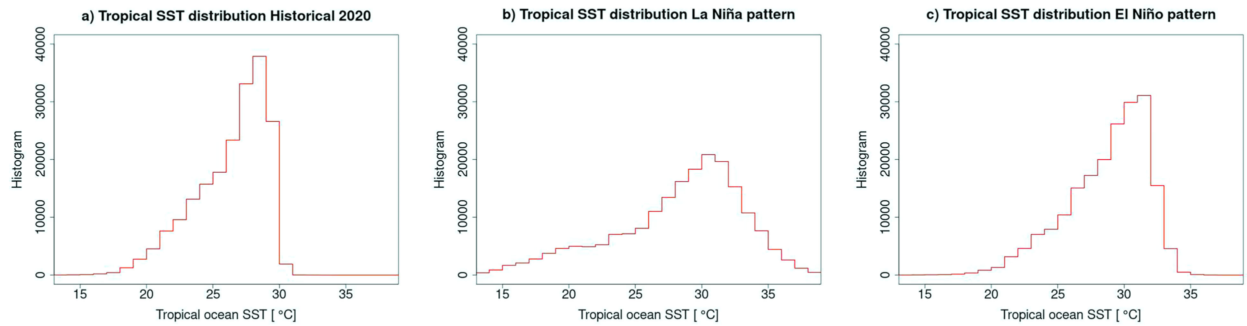

FIG. 9. Tropical SST distributions of the three experiments based on yearly mean data of the 5-km resolution experiments, i.e., each count is a yearly mean SST value of an ocean grid box between 30°S and 30°N. For the computation of the histograms, the 5-km resolution data were regridded to the 25-km resolution model grid using a conservative area-weighted regridding scheme.

and eastern Pacific (Fig. 8). In the 5-km resolution simulation, there is actually an increase in global-mean low cloud cover by 0.9% in the La Niña–like warming simulation and a decrease by 3% in the El Niño–like warming simulation. Here, low cloud cover is defined to include clouds between 1000 and 800 hPa using a maximum overlap assumption (Tompkins and Di Giuseppe 2015).

A response in the tropical Pacific analogous to that in the La Niña–like warming simulations presented here has previously been detected and discussed in investigations of historical warming patterns and related cloud responses (Fueglistaler 2019; Andrews et al. 2022). Fueglistaler (2019) reported that tropical average shortwave cloud radiative effect (SWCRE) anomalies observed by CERES/EBAF version 4 (Loeb et al. 2018) are largely explained by the difference between tropical average sea surface temperature and the warmest 30% of the SSTs. The shapes of the SST distributions are related to the observed variations in boundary layer capping strength over the eastern tropical Pacific. The capping strength, in turn, modulates cloud fraction changes over the colder waters in the tropics which dominate variations in the SWCRE (Fueglistaler 2019). The connection between the warm western Pacific SSTs and the capping strength over the colder eastern Pacific comes about because temperature gradients in the midtroposphere are relatively weak in the tropics. The warmest regions where most deep convection occurs exert a strong control on the tropical average free-tropospheric temperature profile across the whole of the tropics, including the eastern Pacific subsidence areas. By contrast, the boundary layer is strongly impacted by the local surface temperatures. Therefore, over the colder waters of the eastern Pacific, the capping strength increases when surface temperatures cool and free-tropospheric temperatures, influenced by the western Pacific deep convective regions, warm as in the case of the La Niña–like warming simulation.

Tropical (30°S–30°N) SST distributions are displayed in Fig. 9 for the 5-km resolution simulations (each count represents a 25-km resolution grid box of yearly mean SSTs, regridded from the 5-km resolution model simulation). The histograms show that in both the El Niño–like warming simulation and the La Niña–like warming simulation, the upper tails of the distributions become heavier, but much more so in the latter. Figure 10a confirms that the pattern of change in

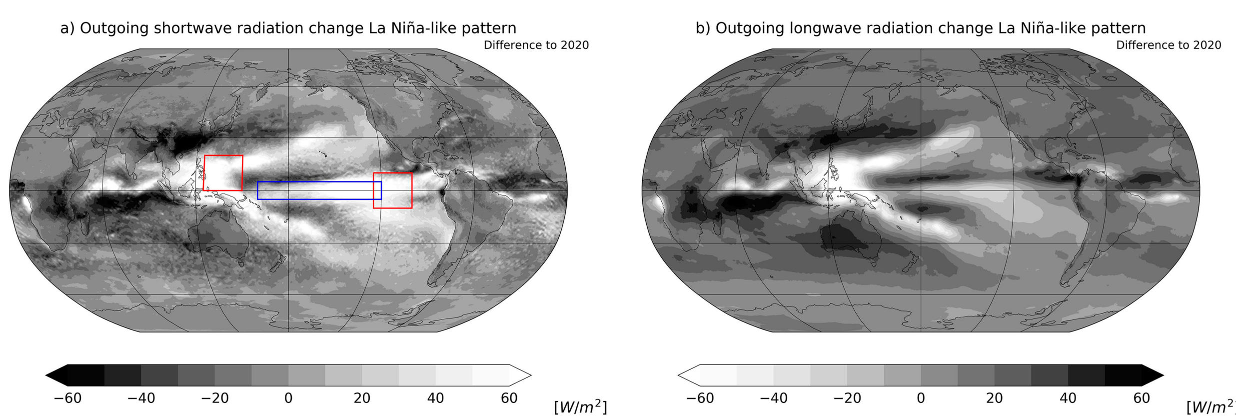

FIG. 10. (a) Change in yearly mean TOA OSR in the La Niña–like warming experiment compared to the historical year 2020 simulation. Different boxes over which area averages are calculated and investigated are indicated: western and eastern Pacific areas (red boxes) and a central Pacific region (blue box). (b) Change in yearly mean TOA OLR in the La Niña–like warming experiment compared to the historical year 2020 simulation. The changes in OLR due to high clouds in deep convective regions are largely offset by opposite changes in OSR.

the OSR in the La Niña–like warming simulation is closely connected to the previously shown change in low cloud cover (Fig. 8c). To investigate changes in atmospheric profiles and other quantities, three regions are defined: areas in the western and eastern Pacific (red boxes in Fig. 10a) and a region in the equatorial central Pacific (blue box in Fig. 10a). The latter region, mainly used to investigate changes in zonal winds, is considered because it is the location commonly studied when characterizing the Pacific Walker circulation. The western Pacific box encompasses the area 125°–150°E, 0°–20°N; it is defined to be located off the equator in order to avoid a significant amount of land points. The eastern Pacific box comprises the region 145°–120°W, 10°S–10°N, and the central Pacific box comprises the region 160°E–120°W, 5°S–5°N.

Moist static energy and saturated moist static energy are useful concepts for elucidating the coupling between convection and its larger-scale environment (e.g., Raymond et al. 2009, for a review). It is beyond the scope of the present article to provide a comprehensive discussion, but instead, we focus here on the most important aspects of profiles of moist static energy and saturated moist static energy over the western and eastern Pacific areas in the different simulations (Fig. 11). In the western Pacific, the changes in profiles mainly reflect a shift in accordance with the regional surface temperature changes for the respective patterns. There are more substantial changes in the upper troposphere that suggest deviations from moist adiabatic lapse rates. Dry static energy profiles (Fig. 11e) reveal that the warming simulations become more stable in the upper troposphere, with the La Niña–like warming simulation much more so than the El Niño–like warming simulation. This impacts upper-tropospheric temperature gradients across the tropics (see also section 5b). Note that the more stable upper troposphere in the La Niña–like warming simulation does not imply reduced high cloud cover in the area (Bony et al. 2016; Wing et al. 2020), on the contrary (Fig. 7). Also, the tropical-mean surface temperatures are very similar in both warming simulations, again emphasizing that the SST distribution has a much heavier upper tail in the La Niña–like warming simulation than in the El Niño–like warming simulation.

Over the eastern Pacific (Figs. 11b,d), the most eye-catching feature is indeed the pronounced stable layer in the upper part of the boundary layer above a shallow mixed layer in the La Niña–like warming simulation. The dry static stability is similar in the midtroposphere for the two warming simulations with again the La Niña–like warming experiment more stable above about 250 hPa (Fig. 11f). In fact, the dry static energy profiles are very similar in the midtroposphere in absolute terms in the two warming simulations, suggesting that they are related to the tropical-mean temperatures. In the western Pacific, however, the dry static energy profile of the La Niña–like warming simulation is warmer than the one of the El Niño–like warming experiment, implying that temperature gradients over the Pacific are not zero even in the midtroposphere in that case. One should note that in the tropics, relatively small temperature gradients can induce considerable large-scale circulations.

There are no other obvious reasons for the increased cloud cover over the eastern Pacific apart from the more pronounced capping strength in the La Niña–like warming simulation: no distinct strengthening of wind speeds or surface latent heat fluxes can be detected over the considered region, suggesting that the more pronounced inversion is the main cause for trapping moisture in the boundary layer and enhancing cloud cover. Qualitatively, the behavior of the 25-km resolution simulations is quite similar to the 5-km resolution experiments, but there are some quantitative distinctions which are potentially important. The differences between the two resolutions and configurations will be discussed in more detail in the next paragraph.

d. Differing behavior between convection-permitting and parameterized convection simulations

From Table 1, it can be inferred that although the climate sensitivity estimates are very similar for the 5- and 25-km resolution experiments, there are differences in the TOA OSR and OLR fluxes, and these differences compensate each other. More precisely, in the 25-km resolution simulations with parameterized convection, the OSR reduces more in the warming simulations, but OLR increases more, i.e., less sunlight is reflected and more heat is radiated into space in the 25-km warming experiments. In terms of cloud cover, this translates into the fact that both low cloud cover and high cloud cover reduce more in the 25-km resolution simulations compared to the 5-km resolution simulations.

It is interesting to note that also in recent warming trends derived from observations, the aforementioned compensation can be seen to some extent: the observed warming trend is mainly due to a reduction in OSR which is partially offset by an increase in OLR (Dübal and Vahrenholt 2021). As discussed in section 3b, in this context, the increase in OLR is expected due to the global-mean temperature increase (Jeevanjee and Fueglistaler 2020).

The patterns of change are not fundamentally different between resolutions, but there are some notable distinctions. The difference between resolutions is larger for the La Niña–like warming simulation than for the El Niño–like warming simulation; therefore, we restrict the discussion to the former for the sake of brevity. One could speculate that this is related to the fact that there are stronger changes in circulations in the La Niña–like warming simulation than in the El Niño–like warming simulation, and the coupling between circulation and moist convection is a main difference between the lower-resolution parameterized convection simulations and the higher-resolution convection-permitting simulations.

The 25-km resolution warming simulations tend to dry somewhat more strongly in the midtroposphere (Figs. 6d,f). The difference in high cloud changes is quite distinctive over the western tropical Pacific: the high cloud cover increases are more pronounced in the 5-km resolution simulation than in the 25-km resolution simulation (Figs. 7c,d), consistent with the idea that the coupling between convection and circulation is more intimate in the 5-km resolution model. On the other hand, the increases in low cloud cover over the eastern tropical Pacific are not obviously stronger in the 5-km resolution simulation than in the 25-km resolution simulation (Figs. 8c,d), possibly because low clouds are mostly parameterized at both

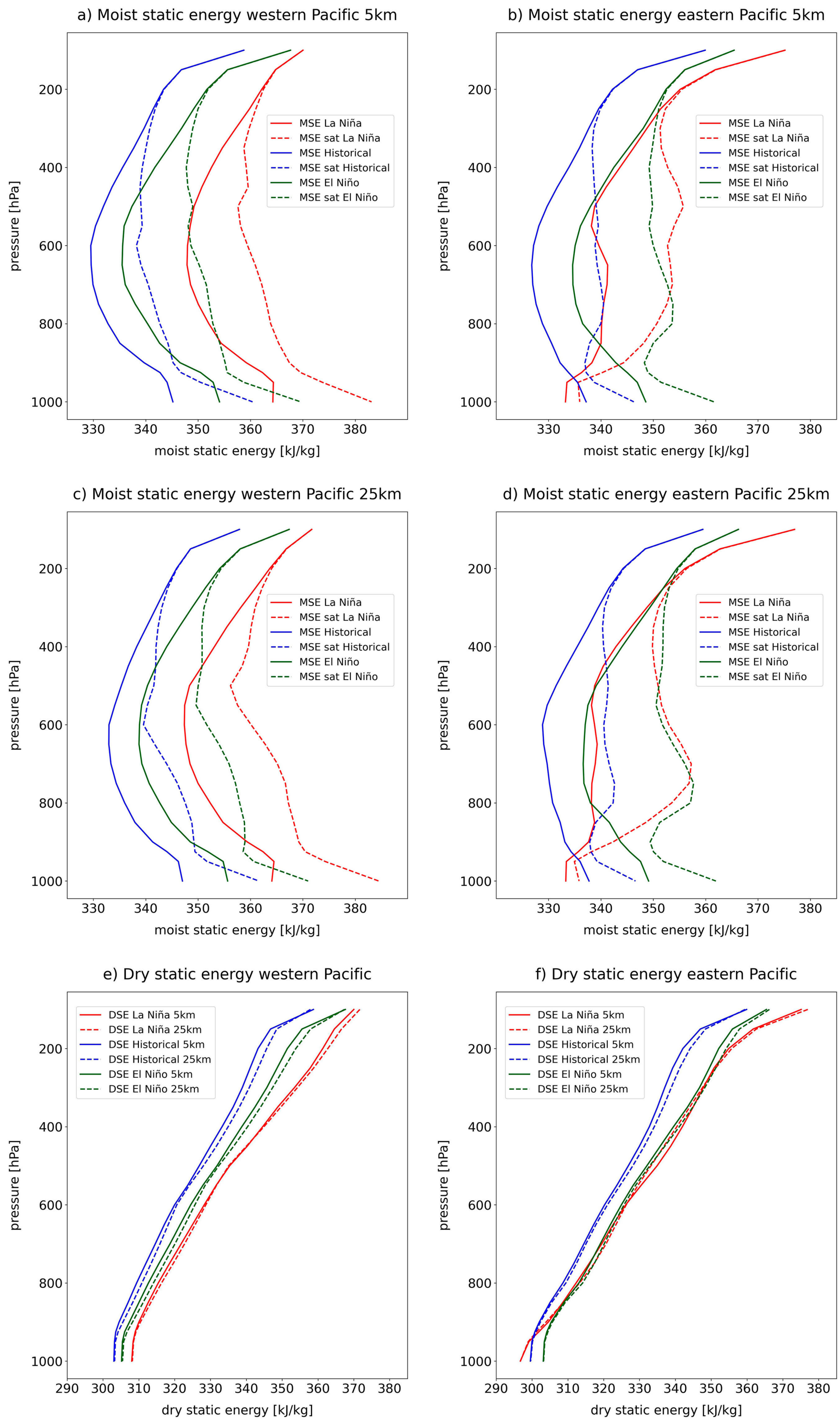

FIG. 11. Mean moist static energy and saturated moist static energy profiles for the western Pacific and eastern Pacific areas as defined in Fig. 10a. Both the results from the (top) 5-km resolution and (middle) 25-km resolution experiments are shown. Solid lines represent moist static energy and dashed lines saturated moist static energy in the upper two rows. The different colors correspond to the different experiments. (bottom) Mean dry static energy profiles at 5- and 25-km resolution for the western Pacific (bottom-left panel) and the eastern Pacific regions (bottom-right panel).

resolutions. The differences in low cloud cover seem to be more subtle. In fact, some of the differences in OSR may actually be due to medium and high clouds rather than low clouds. This is plausible given that the differences in model formulation related to the shallow convection scheme are modest between the two resolutions, as noted in section 2.

With regard to the atmospheric profiles in the western and eastern Pacific (Fig. 11), they confirm the stronger midtropospheric drying in the 25-km warming simulations compared to the corresponding 5-km simulations. This is particularly notable in the lower part of the midtroposphere between about 800 and 600 hPa, part of which will occasionally be in the cloud layer. In the western Pacific deep convective region, the 25-km resolution simulation is warmer in the midtroposphere and upper troposphere than in the 5-km resolution simulation. This is true not only for the La Niña–like warming simulation but also for the El Niño–like warming simulation and the historical year 2020 control. In the eastern Pacific subsidence region, there is more warming around 700 hPa, less around 400, and more above about 250 hPa in the 25-km resolution La Niña–like warming simulation compared to the 5-km resolution La Niña–like warming simulation. As already mentioned, the dry static energy profiles of the La Niña–like warming simulation and the El Niño–like warming simulation are close in the eastern Pacific between 850 and about 250 hPa, particularly for the 25-km resolution simulation for which the profiles are almost identical in this altitude range (Fig. 11f).

The moist static energy profiles in the eastern Pacific are quite well mixed through the midtroposphere in both resolutions but at a higher value in the 5-km resolution simulation mainly due to the higher moisture content. So in terms of dry static stability, the eastern Pacific boundary layer capping strength is stronger in the 25-km resolution simulation, but in terms of moist static stability, it is stronger in the 5-km resolution simulation.

The structure of the atmospheric profiles and the connection between the western and eastern tropical Pacific are influenced by the atmospheric circulation. In the next section, we will investigate aspects of the circulation and the coupling between moist convection, clouds, and the large-scale atmospheric circulation. Before focusing more specifically on the tropical Pacific region, some general features of changes in the tropical circulation under the different warming patterns are investigated.

4. Changes in the tropical circulation and related convection–circulation interactions

Idealized studies have investigated changes in the tropical circulation under warming (Jenney et al. 2020; Jeevanjee 2022). Here, we want to test some of those ideas under more realistic conditions using kilometer-scale global simulations and exploring the dependence on the pattern of warming. Starting from these more general considerations, we will then go on to examine changes in the circulation over the tropical Pacific more specifically and how these changes may relate to changes in clouds and convection in the region.

Changes in the tropical circulation under different warming patterns

There are different possible definitions of the strength of the tropical circulation, and what definition to consider depends on the research question. One definition that is particularly relevant for convection and rainfall processes is the strength of the convective mass flux in the tropics (Held and Soden 2006; Jeevanjee 2022). In the tropics, the convective mass flux is approximately the upward mass flux (Gross et al. 2018).

Since we will only use daily mean data, it is justifiable to evoke the approximation $\omega \approx -w \times g \times \rho$, where ω is the vertical pressure velocity, g is the acceleration due to gravity, w is the vertical velocity, and ρ is the air density. The (upward) mass flux is then defined as

$$\text{mass flux} = \frac{-\omega}{g}.$$

For the vertical pressure velocity, we only consider the resolved, grid-scale quantity. This will give a reasonable quantitative picture in the case of the 5-km resolution convection-permitting simulations. For the 25-km parameterized convection model, a large part of the convective mass is subgrid, and the explicit mass flux only provides a qualitative measure.

When describing changes in the upward mass flux with warming, it is important not only to consider the mean over the areas over which the mass flux is upward but also to take into account that the extent of these areas or the frequency of upward motion can change. In the following, we restrict the investigation to the tropics which is defined to stretch from 30°S to 30°N and, for simplicity, to normalize the total area of the tropics to 1. In other words, assume that the upward mass flux is constant in the tropics (C kg m^{-2} s^{-1}), then we define the total upward mass flux in the tropics (C kg s^{-1}). If the upward mass flux is not constant, then the values will be area-weighted in such a way that the total area of the tropics is normalized to 1. The analogous weighting and normalization are applied in time, and in the following, it is understood that both the area over which upward mass fluxes are considered as well as their frequency of occurrence (i.e., the frequency when the mass flux is upward and not downward) are taken into account.

$$\text{Tropical mass flux} = \sum_{i=1}^{n\_\text{days}} \sum_{k=1}^{n\_\text{grid\_cells}} \frac{1}{n\_\text{days}} a_k m_{ik}^{\text{up}}, \tag{1}$$

where a_k are the area weights such as

$$\sum_{k=1}^{n\_\text{grid\_cells}} a_k = 1, \tag{2}$$

and m_{ik}^{up} is the respective daily mean mass flux of the grid cell if it is upward and zero otherwise. Only grid cells in the tropics are considered, i.e., n_grid_cells is the number of grid cells between 30°S and 30°N and n_days = 366 is the number of days of the year. With this definition, the values for the changes in the tropical upward mass flux for the different warming simulations are summarized in Table 2.

TABLE 2. Changes in tropical (30°S–30°N) upward mass flux for the different warming experiments and resolutions; the percentage changes in brackets are computed relative to the respective historical 2020 experiments. The daily mean values are area weighted in such a way that the total area of the tropics is normalized to 1, and an analogous weighting and normalization are applied in time. This way both the extent of the area over which the mass flux is upward is considered as well as the frequency.

Warming experiment	Area weighted upward mass flux change, 500 hPa	Area weighted upward mass flux change, 850 hPa
5-km La Niña–like pattern	-0.467×10^{-3} kg s^{-1} (-11.84%)	$+0.174 \times 10^{-3}$ kg s^{-1} ($+3.39\%$)
25-km La Niña–like pattern	-0.282×10^{-3} kg s^{-1} (-9.18%)	$+0.163 \times 10^{-3}$ kg s^{-1} ($+4.43\%$)
5-km El Niño–like pattern	-0.256×10^{-3} kg s^{-1} (-6.49%)	-0.021×10^{-3} kg s^{-1} (-0.41%)
25-km El Niño–like pattern	-0.171×10^{-3} kg s^{-1} (-5.56%)	$+0.091 \times 10^{-3}$ kg s^{-1} ($+2.47\%$)

The absolute values for the 5-km resolution historical 2020 simulation are 3.943×10^{-3} at 500 hPa and 5.138×10^{-3} kg s^{-1} at 850 hPa; the corresponding numbers for the 25-km resolution historical 2020 simulation are 3.073×10^{-3} at 500 hPa and 3.682×10^{-3} kg s^{-1} at 850 hPa.

Jenney et al. (2020) investigated changes in the strength of the tropical circulation under warming using radiative–convective equilibrium experiments, i.e., prescribing uniform SSTs and incoming solar radiation, no rotation, and no land. Key points from their study with regard to the mass flux are that (i) the change in upward mass flux is somewhat ambiguous in the midtroposphere and lower troposphere, (ii) the area of the upward mass flux decreases, and (iii) the strongest updraft speeds intensify under warming. Regarding the first point, Jenney et al. (2020) actually find an increase in upward mass flux in the midtroposphere and lower troposphere when changing the SSTs from 295 to 300 K. Also, the strengthening of the strongest upward mass fluxes occurs only when changing the SSTs from 295 to 300 K in their study, not when changing the SSTs from 300 to 305 K. Jeevanjee (2022) noted that changes in cloud base mass flux, roughly changes of upward mass flux below about 800 hPa, are not robust across different models and simulations, mainly because not all water vapor lifted above cloud base necessarily condenses and precipitates to the surface. From the study by Jenney et al. (2020), one should also observe that there are considerable differences between the behavior of mass flux and vertical velocity under warming, an aspect that is confirmed by our analysis but not discussed here for the sake of brevity.

It is interesting to compare these findings with the ones in the present study using a more realistic setup, in particular with the behavior of the 5-km resolution global convection-permitting simulations, and to also consider the dependence on the warming pattern. In broad agreement with the more idealized studies, the upward mass flux in the midtroposphere decreases, more so in the La Niña–like warming simulation than in the El Niño–like warming simulation (Table 2). This is true not only at 500 but also at 700 hPa, for example (not shown). The situation is much less clear at 850 hPa where at 5-km resolution, there is a small decrease for the El Niño–like warming simulation, but there is an increase of the upward mass flux in the La Niña–like warming simulation. The 25-km resolution simulations show increases in the resolved 850-hPa upward mass flux for both warming patterns.

It is plausible to interpret the differences between the two warming patterns in light of the arguments discussed in Jenney et al. (2020). They suggested that decreases in tropical ascent areas are balanced by increases in latent heating in convective regions.

The mean rainfall increase over grid cells when and where the vertical pressure velocity at 500 hPa is upward amounts to 3.29% K^{-1} for the La Niña–like warming experiment at 5-km resolution and 4.92% K^{-1} for the El Niño–like warming simulation. If one uses a threshold for the upward vertical pressure velocity at 500 hPa of 0.3 Pa s^{-1}, then the values are 21.1% K^{-1} for the La Niña–like warming experiment and 11.17% K^{-1} for the El Niño–like warming simulation. This indeed corresponds qualitatively to changes in the areas and frequencies of occurrence of the respective events as suggested by Jenney et al. (2020). If one uses a threshold for the upward vertical pressure velocity at 500 hPa of 0.3 Pa s^{-1}, then the corresponding area and frequency is 3.58% of the tropics and of the year in the historical 2020 simulation, 2.86% in the La Niña–like warming simulation and 3.23% in the El Niño–like warming simulation. This is consistent with the idea that stronger increases in rainfall, and therefore latent heating, lead to stronger decreases in tropical ascent areas. If we consider all pressure velocities at 500 hPa that are upward, then the corresponding numbers are 25.49% for the historical 2020 simulation, 25.31% in the La Niña–like warming simulation, and 23.77% in the El Niño–like warming simulation. The precise definition of what convective mass flux means matters when it comes to the qualitative behavior of rainfall changes and related characteristics in the different warming patterns.

Jenney et al. (2020) also point out that the changes in upward mass flux in their warming simulations are closely related to the humidity and humidity changes in the respective atmospheric column. For example, the strongest increases in upward mass flux are observed in the wettest columns. Better understanding the changes in humidity in the different warming simulations therefore helps better understand the changes in circulation. The increase in vertically integrated water vapor over the tropical belt is 10.49% K^{-1} in the La Niña–like warming simulation at 5-km resolution and 7.8% K^{-1} for the El Niño–like warming simulation. Figure 12 shows the yearly mean pattern of the vertically integrated water vapor path for the three simulations. It is apparent that the stronger increase in moisture in the La Niña–like warming simulation compared to the El Niño–like warming simulation is mainly due to the strong increase in humidity in the moist tropical convergence zones (Fig. 12, first row). The close connection to the circulation is obvious from the spatial patterns of the vertical

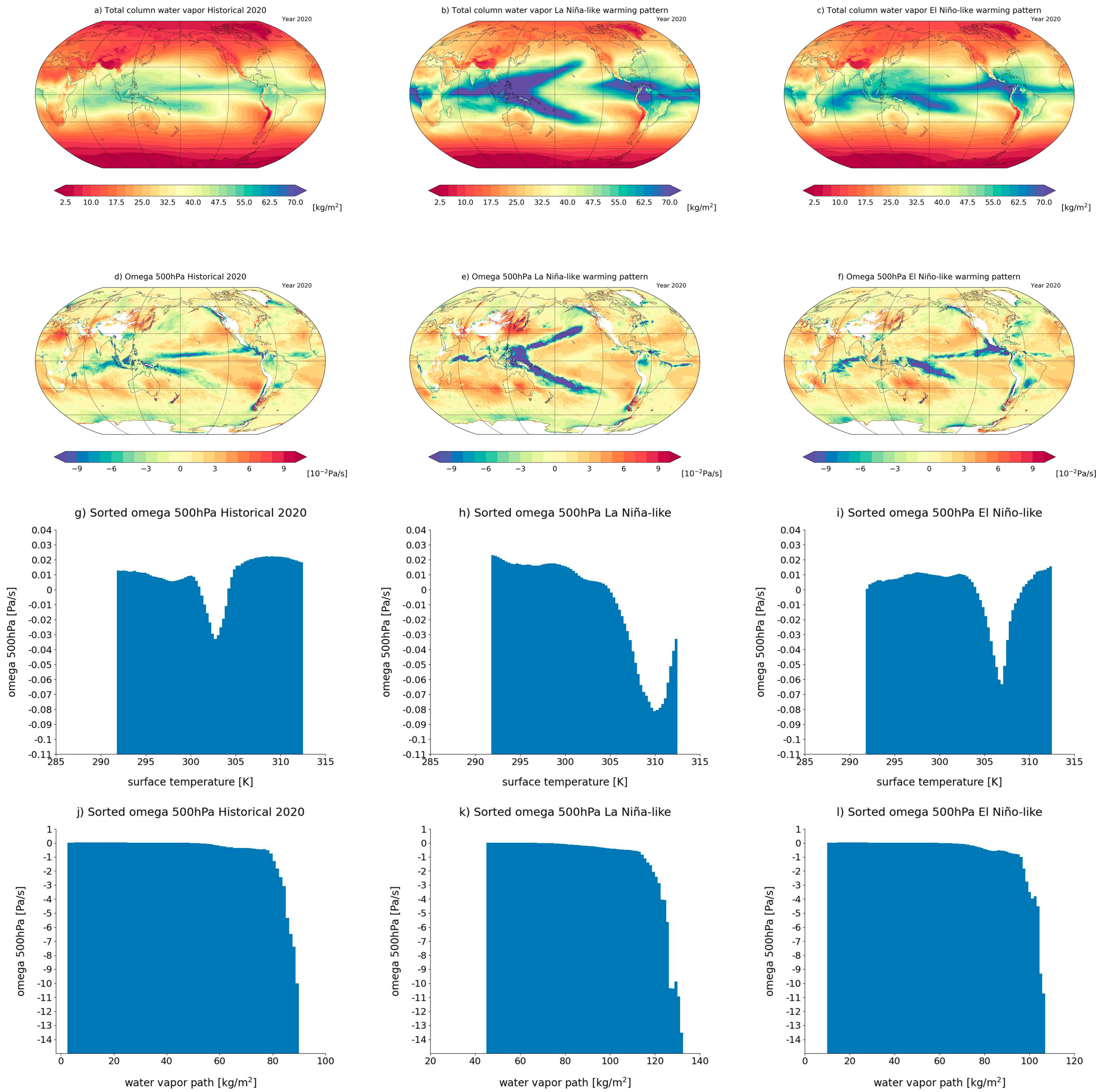

FIG. 12. (first row) Yearly mean vertically integrated water vapor for the historical 2020 simulation at (a) 5-km resolution, (b) the La Niña–like warming pattern simulation, and (c) the El Niño–like warming pattern simulation. (second row) Yearly mean vertical pressure velocity at 500 hPa for the same experiments. For the figures, the values were regridded to the 25-km model grid using a conservative area-weighted regridding scheme. Where the 25-km resolution orography intersects with the 25-km yearly mean 850-hPa geopotential height field, the area is left white so that the figures are not dominated by local orographic effects. (third row) Daily mean vertical pressure velocity at 500 hPa over the tropics sorted in bins of surface temperature for the 5-km resolution experiments. The values were first regridded to the 25-km resolution model grid using a conservative area-weighted regridding scheme. (fourth row) Daily mean vertical pressure velocity at 500 hPa over the tropics sorted in bins of vertically integrated water vapor path for the 5-km resolution experiments. The values were first regridded to the 25-km resolution model grid using a conservative area-weighted regridding scheme.

pressure velocity at 500 hPa (Fig. 12, second row). The strongest increases in vertical pressure velocity, and thus mass flux, at 500 hPa are collocated with areas of strongest humidity increases although the zones of distinct pressure velocity increases are narrower because they are related to moisture increases via a power-law relation (Zhang and Fueglistaler 2020; Neelin et al. 2009). This is confirmed when sorting daily mean values of vertical pressure velocity at 500 hPa with regard to surface temperature and vertically integrated water vapor bins (Fig. 12, third and fourth rows). Each vertical bar

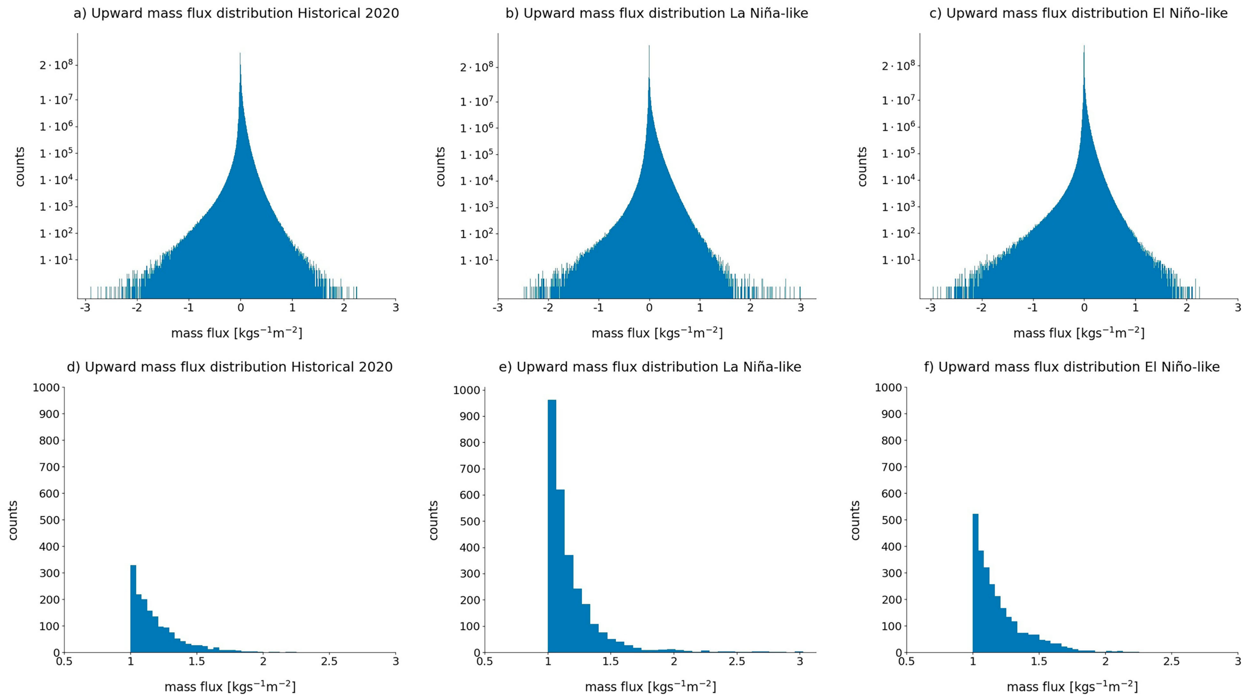

FIG. 13. (top) Histograms of resolved tropical mass flux at 500 hPa for the 5-km resolution simulations. Each count is a daily mean value for one particular grid box in the tropical band from 30°S to 30°N. (bottom) Zoom on the upper tails of the histograms.

represents the mean value of vertical pressure velocity at 500 hPa over the respective bin. It is clear that the relationship between SSTs and the regions of strongest updrafts is complex and not simply governed by an absolute threshold value. The vertical pressure velocity is not monotonically related to surface temperature, and the clearly identifiable deep convective regimes are not tied to a fixed surface temperature (Fig. 12, third row). Humidity and circulation regimes are important factors in how SSTs couple to deep convection (see, e.g., Lindzen and Nigam 1987; Neelin and Held 1987; Sobel 2007; Back and Bretherton 2009; Zhang and Fueglistaler 2020, for more detailed discussions). In contrast, the more moisture there is in an atmospheric column, the stronger the upward mass flux (Fig. 12, fourth row).

Histograms of the tropical mass flux at 500 hPa for the 5-km resolution simulations show how the distributions change in the different warming simulations (Fig. 13). As one would expect from the previous discussion of the changes in humidity in the warming simulations, the upper tail of the mass flux distribution increases in the La Niña–like warming simulation, and the same is true for the El Niño–like warming simulation but to a lesser degree (Fig. 13, second row). Thus, the tropical circulation does not change uniformly, but the distributions of vertical motions alter, and these changes in characteristics impact changes in clouds and convection.

5. Circulation, clouds, and convection over the tropical Pacific

As discussed in section 3, when it comes to the climate change response, in particular the changes in clouds and convection, the tropical Pacific is an important region. There are key differences between the two warming simulations not only with regard to the cloud response but also with regard to how the tropical circulation changes that are related to the tropical Pacific. In the La Niña–like warming simulation, the vertical tropical circulation in the midtroposphere generally slows more strongly than in the El Niño–like warming experiment, but the strongest updrafts strengthen, for example, in the warm and moist regions of the western Pacific (section 4) where also the cloud responses differ markedly. So what role does the atmospheric circulation play in the tropical Pacific and how are these changes related to clouds and convection? The question is first addressed in the historical simulations (section 5a) and then investigated in the light of the two warming experiments (section 5b).

a. Circulation over the tropical Pacific in the historical simulations

We first would like to establish more specifically that there is indeed a relationship between the circulation and convection in the tropical Pacific region. In this section, we restrict to the historical year 2020 simulations, and only daily mean values will be considered in the analysis. We refer again to Fig. 10a for the definition of different regions over which averages are investigated: the western Pacific and eastern Pacific areas (red boxes) and the mid-Pacific to eastern Pacific equatorial region (blue box), called the central Pacific region in the following for simplicity. The latter area is often studied in connection with the Pacific Walker circulation and will be used to compute area means of zonal winds.

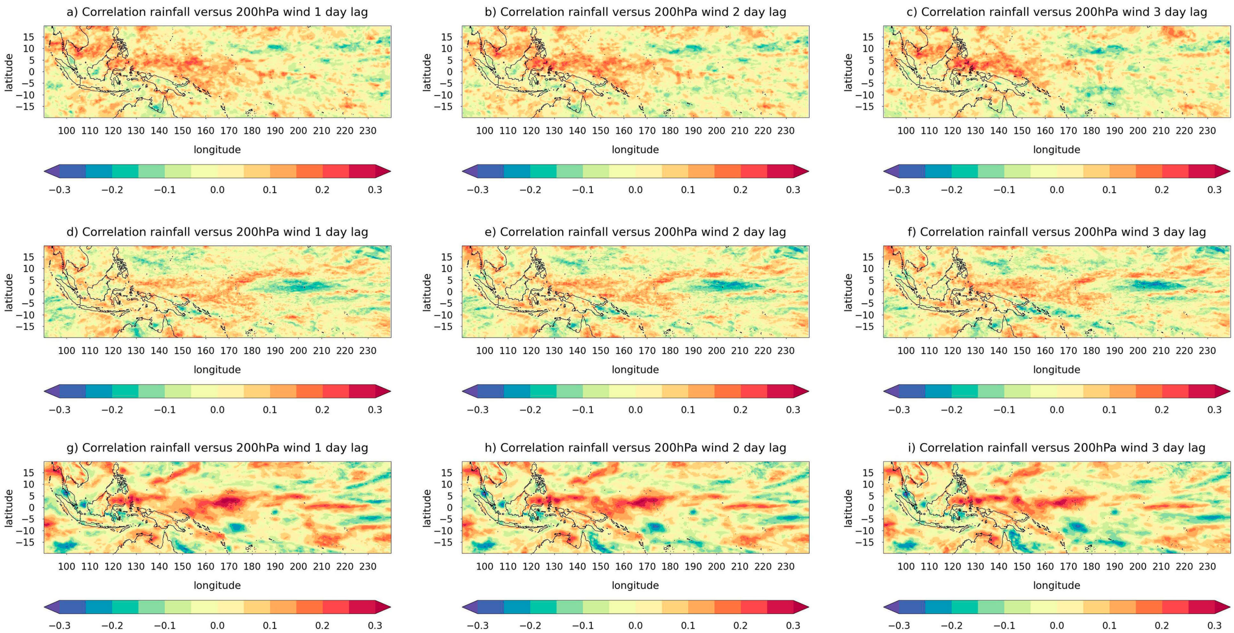

FIG. 14. Correlations between daily mean rainfall and the daily mean zonal wind at 200-hPa averaged over the central Pacific region (blue box in Fig. 10a) calculated for every grid box of the area 20°S–20°N and 90°E–120°W. (top) Data from GPM rainfall observations and ERA5 200-hPa zonal wind are used. Correlations are calculated with the wind lagging rainfall for 1, 2, and 3 days. For both the rainfall and the wind data, a seasonal cycle was removed using a Savitzky–Golay filter of order 3 with a window size of 120 days. (middle) The same correlations but based on the 5-km resolution experiments. For the calculation of the correlations, the rainfall data were first regridded to a 25-km resolution model grid using a conservative area-weighted regridding scheme. For both the rainfall and the wind data, a seasonal cycle was removed using a Savitzky–Golay filter of order 3 with a window size of 120 days. (bottom) As in (middle), but for the 25-km resolution experiments. For both the rainfall and the wind data, a seasonal cycle was removed using a Savitzky–Golay filter of order 3 with a window size of 120 days.

First, correlations are computed between the wind at 200 hPa averaged over the central Pacific region and rainfall at every grid point in the area 20°S–20°N and 90°E–120°W (Fig. 14). As already mentioned, only daily mean values are used, but different lags between rainfall and the 200-hPa wind are considered, from a 1-day lag to a 3-day lag, acknowledging that certain parts of the domain are geographically far away from the central Pacific region. The correlations are calculated for ERA5 and the Global Precipitation Measurement (GPM; Huffman et al. 2019) mission dataset (top row), the 5-km resolution historical year 2020 simulation (middle row), and the 25-km resolution historical year 2020 experiment (bottom row).

Given that the western edge of the central Pacific region is at 160°E and extends to 120°W, it is quite remarkable that the strongest positive correlations with rainfall are identified quite far west over or close to the Maritime Continent even though, north of the equator, the Pacific ITCZ can reach all the way to Central America. In ERA5 and GPM, it is apparent how the strongest positive correlations move somewhat westward as the lag is increased (Fig. 14, top row). This feature is less obvious in the 5-km resolution model simulation. The correlation pattern is fairly independent of the lag, and there is a branch of positive correlations north of the equator that reaches rather far east (Fig. 14, middle row). This is related to the somewhat erroneous structure of the ITCZ in the 5-km resolution experiment which exhibits a too strong and static oceanic convergence zone in the region. Apart from that, the overall structure and magnitude of the correlations are sensible. The 25-km resolution simulation actually tends to produce somewhat stronger positive correlations than the 5-km resolution model especially near the equator in this analysis (Fig. 14, bottom row). However, if the 5-day integrated western Pacific area-mean rainfall is correlated with the mean 200-hPa zonal wind over the central Pacific in an analogous way, then the correlations are considerably weaker in the 25-km resolution simulation with parameterized convection than the convection-permitting 5-km resolution experiment (not shown). This suggests that on short time scales and near-gridpoint scales, the parameterized convection model can produce quite strong dynamical responses to convection and latent heating, but on longer time scales and larger spatial scales, the intermittency of the convection scheme hampers this ability.

To further investigate the connection between latent heating and the circulation over the tropical Pacific, the relationships between different quantities are scrutinized by plotting them against each other in scatterplots and calculating corresponding correlations (Fig. 15). The significance of the correlations is assessed against the null hypothesis that there is no correlation between the variables. The latter is quantified by randomizing the values 10 000 times, computing the correlation between the randomized points each time, and taking the

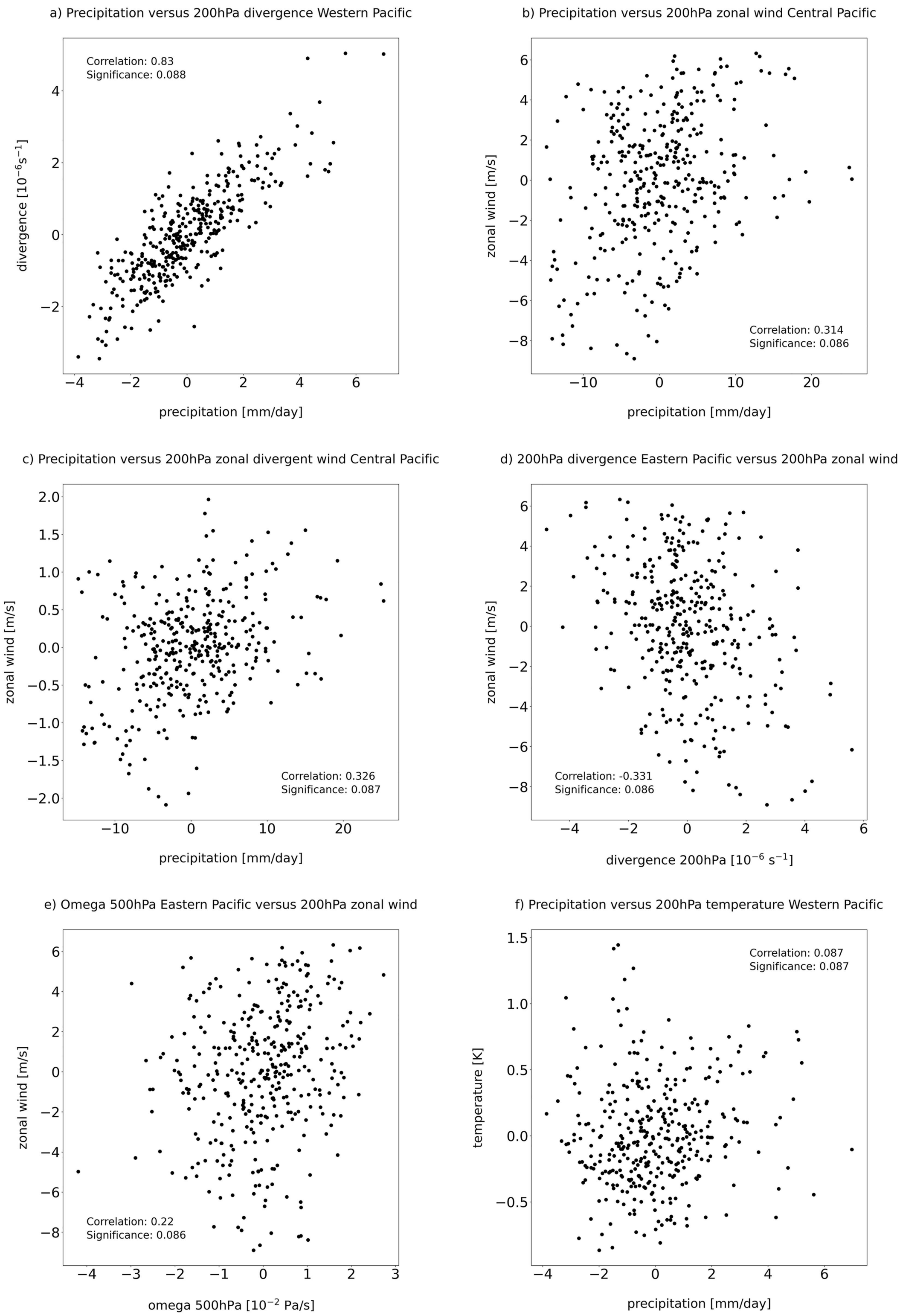

FIG. 15. (a) Scatterplot of daily mean rainfall averaged over the western Pacific region (see Fig. 10a for the definition of the regions) and daily mean divergence at 200 hPa averaged over the western Pacific area based on the 5-km resolution historical 2020 simulation. (b) Scatterplot of 5-day integrated mean rainfall over the western Pacific region vs mean 200-hPa zonal wind over the central Pacific. A lag of 3 days is used between the end of the averaging periods of the rainfall data and the wind. (c) As in (b), but with the divergent wind at 200 hPa instead of the full wind field.

95th quantile of these 10 000 correlation values (e.g., Wilks 2011, chapter 5.1). The significance values that are reported in the figure panels are therefore the half-widths of the 90% confidence intervals for the correlations under the null hypothesis. If the correlations computed from the model data are within plus or minus these values, then the null hypothesis that the correlations occur only by chance due to the small sample size cannot be rejected. The quantities that are correlated are daily mean values averaged over large geographical areas. Convection typically takes place on much smaller scales with a high degree of variability in space and time. Here, we try to detect the effect of convection on the larger scales deliberately using a relatively crude methodology. The correlations are not expected to be large in absolute terms, but we argue that most of the correlations presented below are still significant in the defined sense.

To keep the discussion reasonably concise, only the results from the 5-km resolution simulation are shown. Daily mean values of rainfall over the western Pacific area correlated with daily mean values of divergence at 200 hPa over the same region exhibit a very clear and strong relationship (Fig. 15a). This is an important connection and shows that rainfall and latent heating are closely related to the upper-level circulation in the deep convective region even when considering a relatively crude area average and daily mean time scales. The analysis around Fig. 14 revealed that there are correlations between daily mean rainfall in the western Pacific deep convective region and the 200-hPa zonal wind in the central Pacific. When exploring this relationship further, it turns out that the connection becomes stronger when using integrals of rainfall over several days instead of rainfall on a single day. In the scatterplot of Fig. 15b, the 5-day sum of rainfall is related to the 200-hPa zonal wind in the central Pacific with a lag of 3 days. This leads to a clearly significant correlation of 0.314. A seasonal cycle is removed from both the daily mean rainfall and the daily mean zonal wind values using a Savitzky–Golay filter of order 3 with a window size of 120 days. Again one has to keep in mind that rather crude spatial averages are involved in this analysis that does not take into account any specific characteristics of the involved circulations or rainfall patterns.

The correlation between rainfall in the deep convective region of the western Pacific and the central Pacific zonal wind at 200 hPa is further increased when considering only the divergent wind at 200 hPa (Fig. 15c). The divergent wind is usually used in the definition of the Walker circulation over the central Pacific region. In other words, there is a clear connection between rainfall in the western Pacific and the upper branch of the Walker circulation in the central Pacific in the 5-km resolution historical year 2020 simulation. There is also a correlation of similar magnitude between the zonal wind at 200 hPa over the central Pacific and the divergence at 200 hPa over the eastern Pacific (Fig. 15d). This is again an expression of what can broadly be considered the larger-scale circulation over the tropical Pacific. Stronger upper-level zonal winds over the central Pacific Ocean tend to lead to stronger upper-level convergence over the eastern Pacific subsidence areas. It is also possible to relate the 200-hPa zonal winds over the central Pacific to the vertical motion in the midtroposphere in the eastern Pacific area (Fig. 15e). The vertical motion in the midtroposphere has a direct effect on the stability and humidity of the atmosphere, and thus on clouds, via subsidence warming and drying.

No direct connection, however, between rainfall and temperature at 200 hPa can be detected in the western Pacific deep convective area on the considered daily time scale (Fig. 15f). This indicates either that the latent heating at 200 hPa is too small to be detected on the considered spatial scale (Jakob and Schumacher 2008) or that the latent heating does not directly produce positive temperature anomalies in the upper atmosphere on daily time scales. Also, the relation between daily mean rainfall and daily mean OLR or high cloud cover is weak and cannot unequivocally be identified (not shown). Nevertheless, as demonstrated by Fig. 15a, rainfall is closely linked to upper-level divergence in the region and thus likely initiates larger-scale circulations.

Conversely, having established that rainfall and latent heating in the western Pacific is involved in driving larger-scale circulations over the whole of the tropical Pacific, if we want to understand the historical evolution of the climate system and the SSTs in the region, the question arises what controls deep convective rainfall and thus latent heating over the western Pacific. In Fig. 16, the issue is addressed by relating different possible low-level controls of deep convection to rainfall and to each other. As to be expected, there is a connection between divergence at 850 hPa and rainfall. The magnitude of the correlation, however, is quite remarkable given the crude spatial and temporal scales considered (Fig. 16a). There is also a positive, although weaker, correlation between temperature at 850 hPa and rainfall (Fig. 16b). Together with the positive correlation of rainfall with 850-hPa specific humidity (Fig. 16c), this suggests that there is a relationship between low-level moist static energy anomalies and rainfall. In fact, if one considers the vertically integrated water vapor path

⟵
(d) Mean divergence at 200 hPa over the eastern Pacific box vs mean zonal wind over the central Pacific area. (e) Mean vertical pressure velocity at 500 hPa over the eastern Pacific box vs mean zonal wind over the central Pacific area. (f) Mean rainfall over the western Pacific area vs mean 200-hPa temperature over the western Pacific region. In the panels, the correlations are indicated as well as an estimate for a significant correlation. The data are anomalies with regard to a seasonal cycle that was removed using a Savitzky–Golay filter of order 3 with a window size of 120 days. The significance values that are reported in the figure panels are the half-widths of the 90% confidence intervals for the correlations under the null hypothesis. If the correlations computed from the model data are within plus or minus these values, then the null hypothesis that the correlations occur only by chance due to the small sample size cannot be rejected.

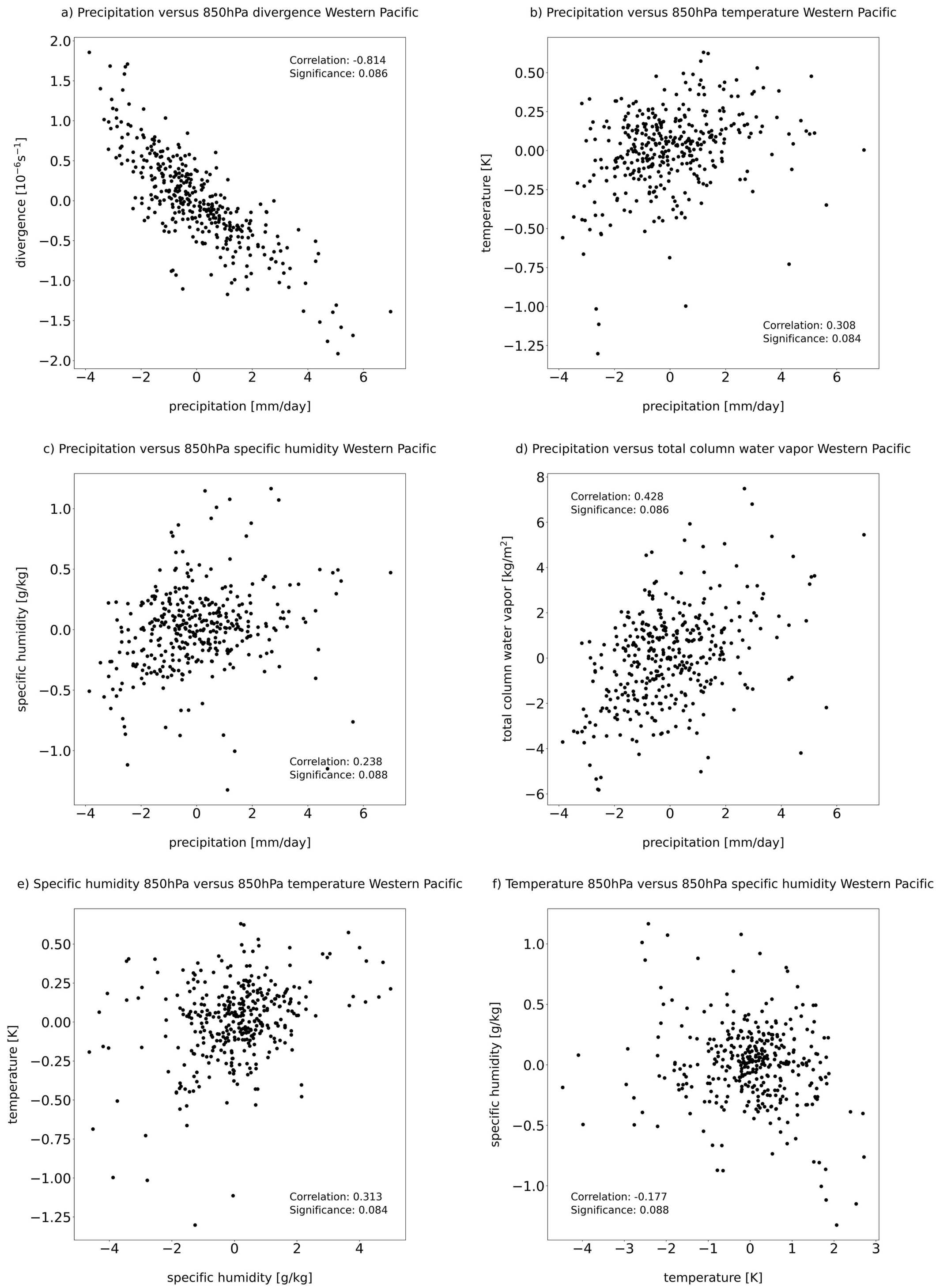

FIG. 16. Scatterplots calculated as in Fig. 15, but for controls of rainfall over the western Pacific. (a) Mean rainfall over the western Pacific area vs mean 850-hPa divergence over the western Pacific region. (b) Mean rainfall over the western Pacific area vs mean 850-hPa temperature over the western Pacific region. (c) Mean rainfall over the western Pacific area vs mean 850-hPa specific humidity over the western Pacific region. (d) Mean rainfall over the western Pacific area vs mean vertically integrated water vapor over the western Pacific region. (e) Scatterplot of 5-day integrated mean 850-hPa specific humidity over the western Pacific region vs mean 850-hPa temperature over the western Pacific. A lag of 3 days is used between the end of the averaging periods of the specific humidity data and the temperature. (f) As in (e), but with the role of specific humidity and temperature reversed. The significance values that are

instead of 850-hPa specific humidity, then the connection to rainfall becomes even stronger (Fig. 16d; Bretherton et al. 2004; Neelin et al. 2009). This leads to the question of whether the relationship between rainfall and humidity is merely a consequence of the relationship between rainfall and low-level temperature or whether humidity has a more active role in governing rainfall and temperature.

When using a 5-day average of 850-hPa humidity to predict 850-hPa temperature 3 days ahead, a significant correlation is found (Fig. 16e). This indicates that the dynamics of moisture actually govern moist static energy anomalies and are not just a consequence of low-level temperature variations. Indeed, when trying to predict 850-hPa humidity 3 days ahead by a 5-day average of 850-hPa temperature, no clearly significant correlation is found, and if any, it is a negative correlation (Fig. 16f). Significant relationships between latent heat fluxes and rainfall using various lags were not found on daily time scales (Hogikyan et al. 2022). Also, correlations between total cloud cover or OLR and rainfall tend to be small and positive, suggesting that anomalously warm conditions tend to come with more moisture and clouds, not less, on the considered daily time scales.

b. *Changes in the circulation over the tropical Pacific under different warming patterns*

In the light of the analysis of connections between rainfall in the western Pacific deep convective regions and the circulation over the central and eastern tropical Pacific areas in the historical simulation (section 5a), the present section investigates changes in the circulation over the tropical Pacific in the different warming pattern experiments. As discussed in the introduction, given that the SSTs are prescribed in the simulations, it is not possible to explain the historically observed warming over the past 30 years based on our experiments. In fact, given that different processes in the climate system interact, it is likely not possible to identify a certain aspect as a unique cause of the particular observed development of the SST pattern. Nevertheless, it is feasible to examine certain mechanisms and interactions and shed some light on their importance and relevance.

Starting first with the lower-tropospheric circulation, the zonal wind at 850 hPa shows a very different pattern of change over the tropical Pacific in the two warming experiments (Fig. 17). In the La Niña–like warming pattern simulations (Figs. 17c,d), a strong intensification of the low-level easterly flow can be seen. The low-level easterlies are usually viewed as being part of the Pacific Walker circulation. It is interesting that even though in the historical simulations, the 25-km resolution experiment did not unequivocally show a weaker relationship between rainfall and winds (section 5a); here, the intensification of the low-level zonal wind in the Pacific equatorial region is distinctly more pronounced in the 5-km resolution convection-permitting simulation compared to the 25-km resolution experiment. This could be very significant in the context of ocean–atmosphere interactions.

In stark contrast, the low-level zonal winds weaken in the El Niño–like warming pattern simulations (Figs. 17e,f). This is of course not unexpected, given the change in the SST patterns (Fig. 2b). However, the west–east temperature gradient does not actually significantly change over the central and eastern tropical Pacific in the El Niño–like warming pattern simulations. The main feature is a somewhat muted warming over the western Pacific deep convective area (section 3d), again suggesting an important role of western Pacific convection and related processes for the zonal circulation over the whole of the tropical Pacific. In the case of the more uniform El Niño–like warming pattern simulations, there is a less distinct but still appreciable difference between the two resolutions in terms of their low-level zonal wind response in the region. In numbers, the yearly mean values of the zonal wind at 850 hPa averaged over the blue box indicated in Fig. 10 for the various simulations are -6.90 m s^{-1} for the historical 5-km resolution simulation, -7.62 m s^{-1} for the historical 25-km resolution simulation, -13.65 m s^{-1} ($+97.83\%$) for the 5-km La Niña–like warming experiment, -10.20 m s^{-1} ($+33.86\%$) for the 25-km La Niña–like warming experiment, -0.21 m s^{-1} (-96.96%) for the 5-km El Niño–like warming experiment, and -2.28 m s^{-1} (-70.08%) for the 25-km El Niño–like warming experiment (in parenthesis are percentage changes in terms of easterly wind relative to the respective historical experiment).

The changes in the upper-level circulation are consistent with the idea that an increased SST gradient over the tropical Pacific induces a Walker-type circulation response with increased low-level easterlies and strengthened upper-level westerlies (Fig. 18). One should note, however, that in the climatology, the upper-level winds are actually mostly easterly over the tropical Pacific (Figs. 18a,b). They turn westerly over the equatorial Pacific area only during the boreal winter months from December to March when the rainfall is most intense over the western Pacific around and close to the Maritime Continent. This climatological picture and the patterns of change in the warming simulations (Fig. 18, second and third rows) indicate the important governing role of deep convection in the western Pacific for the upper-level zonal circulation over the whole of the equatorial tropical Pacific. At upper levels, the difference between the 5-km resolution and 25-km resolution simulation is quite pronounced over central Africa and the Indian Ocean but less so over the tropical Pacific.

The Pacific Walker circulation is usually defined not by the full zonal wind but by the divergent wind only. It is therefore instructive to consider how the zonal component of the divergent wind changes in the warming pattern experiments (Fig. 19). In the historical year 2020 simulations, the 200-hPa divergent zonal wind exhibits the upper-level westerly Walker circulation more clearly, but it is worth noting that in the yearly mean, the westerly divergent flow extends only to about 120°W. Over the main

⟵
reported in the figure panels are the half-widths of the 90% confidence intervals for the correlations under the null hypothesis. If the correlations computed from the model data are within plus or minus these values, then the null hypothesis that the correlations occur only by chance due to the small sample size cannot be rejected.

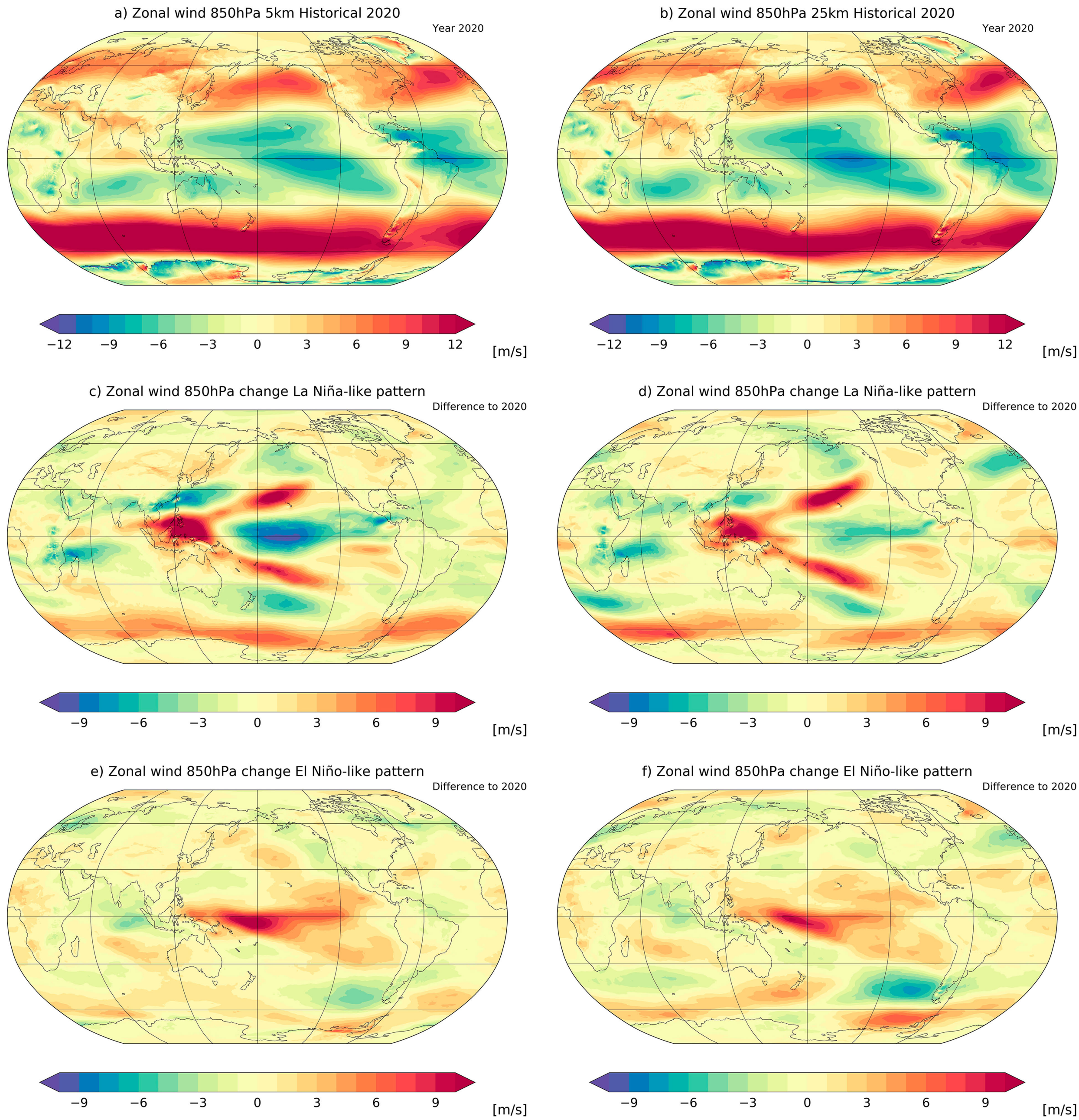

FIG. 17. (a) Yearly mean zonal wind at 850 hPa in the 5-km resolution historical 2020 simulation and (b) yearly mean zonal wind at 850 hPa in the 25-km resolution historical 2020 simulation. Changes in yearly mean zonal wind at 850 hPa for the La Niña–like warming pattern simulations at (c) 5-km resolution and (d) 25-km resolution. Changes in yearly mean zonal wind at 850 hPa for the El Niño–like warming pattern simulations at (e) 5-km resolution and (f) 25-km resolution.

eastern Pacific subsidence areas, the 200-hPa divergent zonal wind is easterly in the yearly mean. In other words, the zonal divergent wind extends from the east of the western Pacific upper-level divergence zone to the west of the eastern Pacific upper-level convergence area.

The response of the zonal divergent wind at 200 hPa in the La Niña–like warming pattern simulations shows a significant expansion of the westerly divergent flow both on the western and the eastern edge of climatological Walker cell (Figs. 19c,d). The signal is considerably stronger in the 5-km convection-permitting simulation than in the 25-km resolution parameterized convection experiment. In the central Pacific, the Walker circulation appears to weaken somewhat in the equatorial area, but this can partly be due to the particular warming pattern which induces pronounced convergence zones from the western tropical Pacific in the northeastern and southeastern

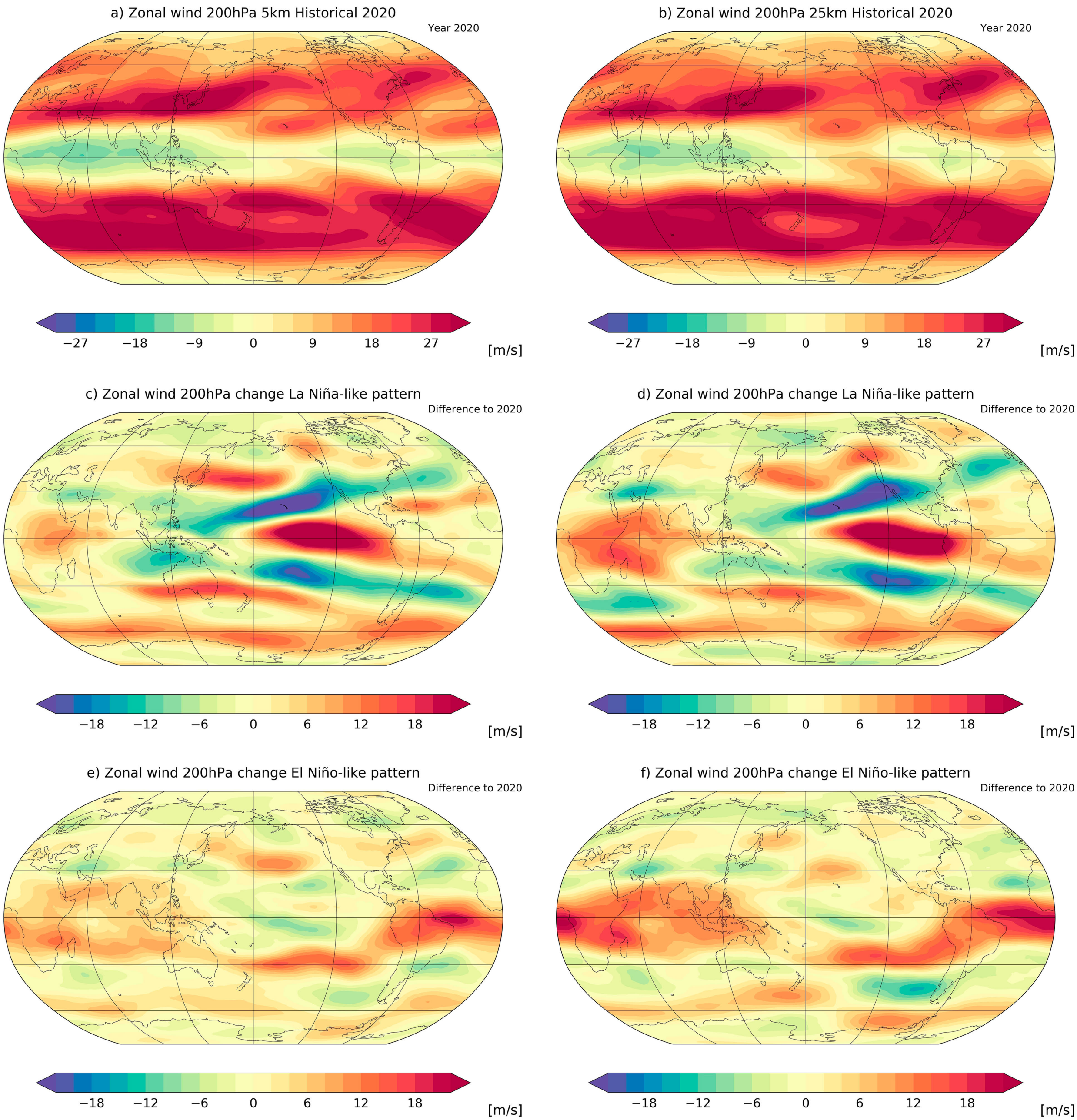

FIG. 18. (a) Yearly mean zonal wind at 200 hPa in the 5-km resolution historical 2020 simulation; (b) Yearly mean zonal wind at 200 hPa in the 25-km resolution historical 2020 simulation. Changes in yearly mean zonal wind at 200 hPa for the La Niña–like warming pattern simulations at (c) 5-km resolution and (d) 25-km resolution; Changes in yearly mean zonal wind at 200 hPa for the El Niño–like warming pattern simulations at (e) 5-km resolution and (f) 25-km resolution.

direction toward the midlatitudes, muting somewhat the divergent upper-level westerly flow in the central Pacific around the equator. In the El Niño–like warming pattern simulations, the upper-level divergent zonal circulation is distinctly weakened, corresponding to a weakening and contracting of the Pacific Walker cell (Figs. 19e,f).

The changes in circulation induce distinct alterations in vertically integrated zonal moisture transport toward and away from the western Pacific deep convective regions (Fig. 20). Climatologically, moisture is transported from the eastern Pacific subsidence areas toward the western Pacific zones of deep convection by the lower-tropospheric flow (Figs. 20a,b). In the La Niña–like warming pattern simulations, this transport is amplified, thus feeding and invigorating deep convective activity in the western Pacific which, in turn, promotes the zonal flow which is responsible for this process (Figs. 20c,d).

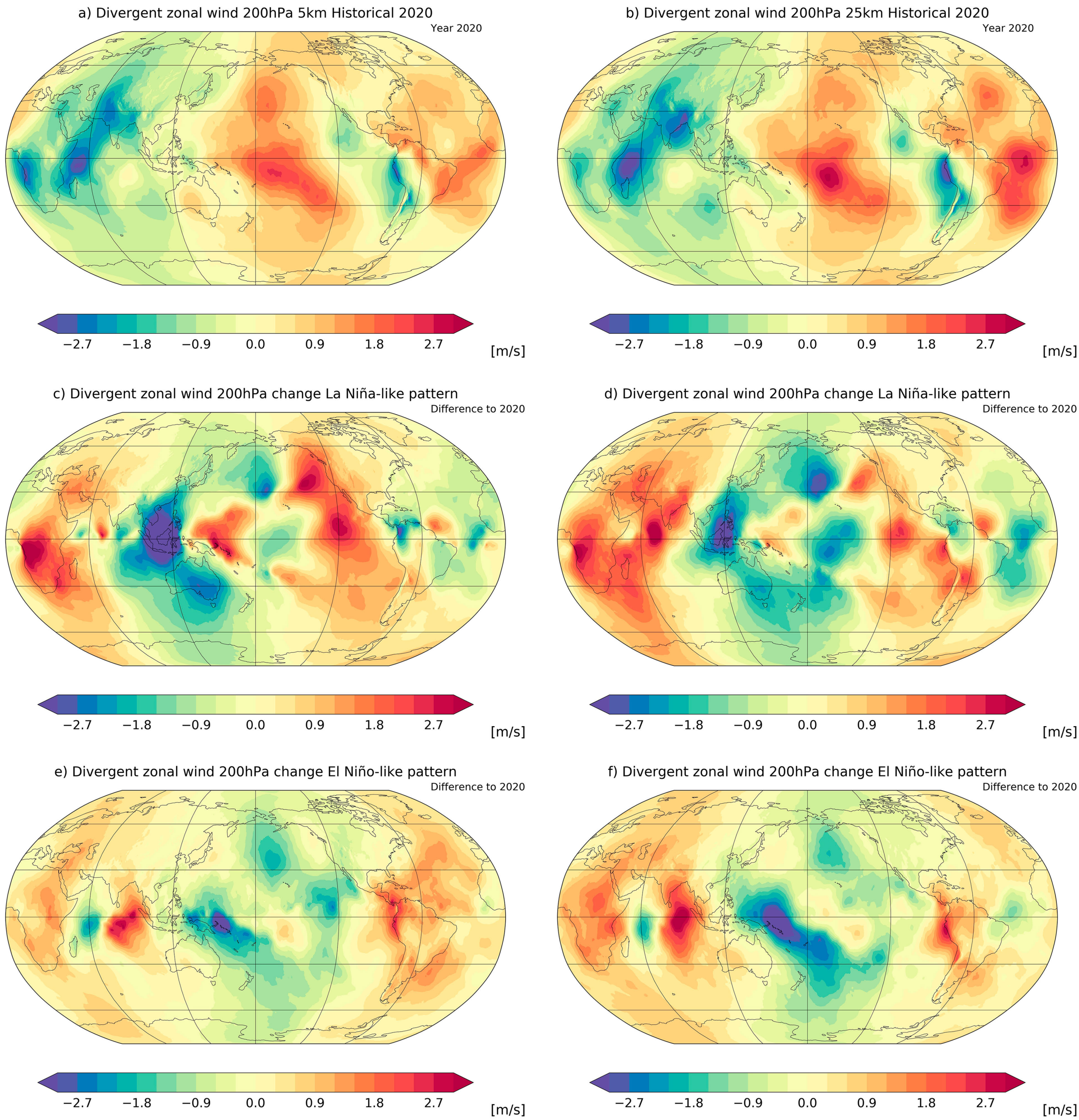

FIG. 19. (a) Yearly mean zonal divergent wind at 200 hPa in the 5-km resolution historical 2020 simulation and (b) yearly mean zonal divergent wind at 200 hPa in the 25-km resolution historical 2020 simulation. Changes in yearly mean zonal divergent wind at 200 hPa for the La Niña–like warming pattern simulations at (c) 5-km resolution and (d) 25-km resolution. Changes in yearly mean zonal divergent wind at 200 hPa for the El Niño–like warming pattern simulations at (e) 5-km resolution and (f) 25-km resolution.

There is thus a positive, large-scale moisture-circulation feedback in which western Pacific deep convection, the zonal circulation, and moisture dynamics work together to intensify all three aspects of the mechanism. While the primary control of the Walker circulation is the east–west surface temperature gradient, the interactions between convection, moisture, low-level convergence, and upper-level divergence over the western Pacific have the potential to provide a positive feedback on the larger-scale zonal circulation. The signal in the moisture transport is distinctly stronger in the 5-km resolution convection-permitting simulation compared to the 25-km resolution parameterized convection experiment, consistent with the lower-tropospheric zonal circulation response. In contrast, in the El Niño–like warming pattern simulations, the easterly moisture transport is weakened, and therefore, the moisture supply to the deep convective western Pacific

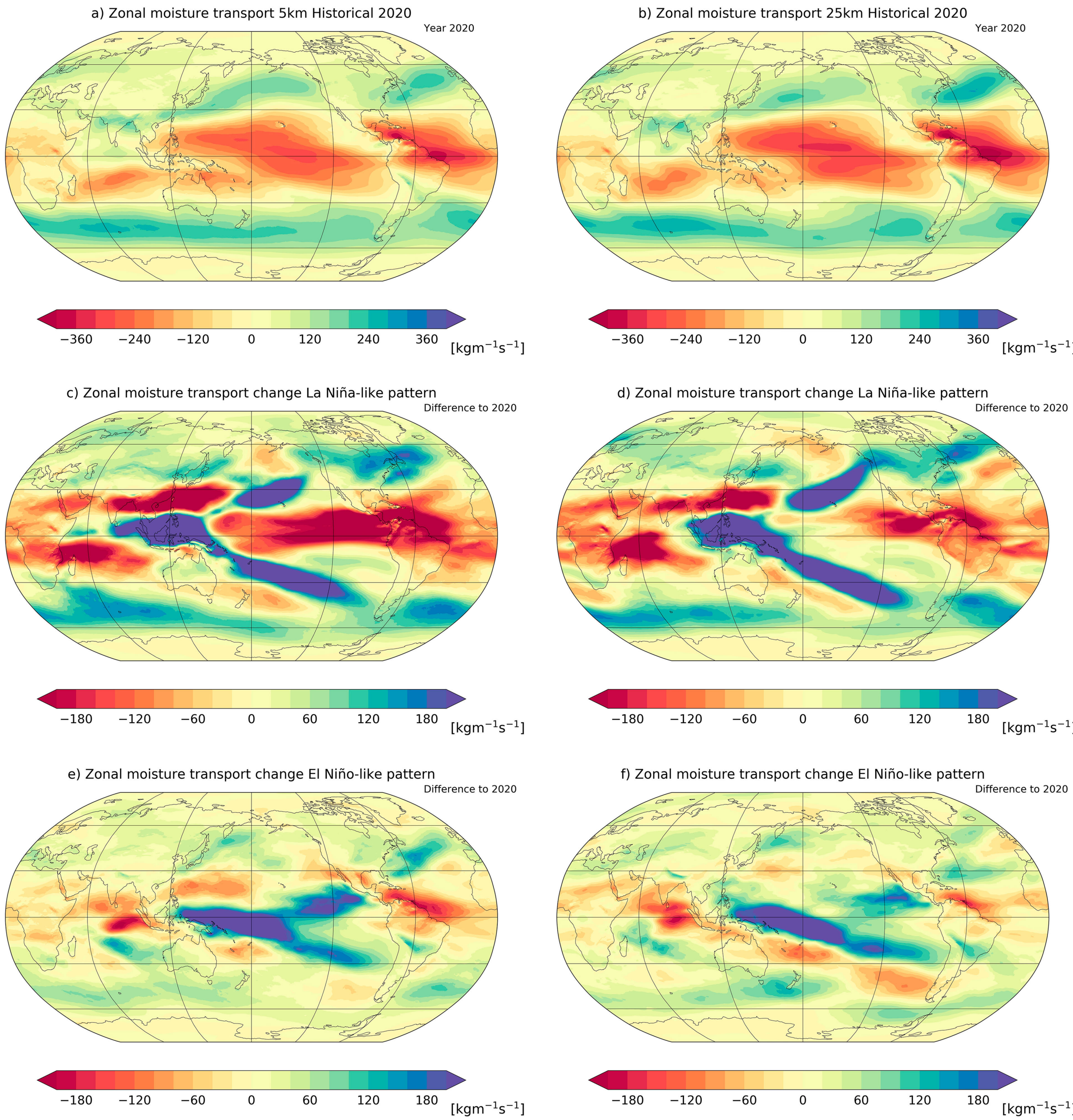

FIG. 20. (a) Yearly mean zonal moisture transport in the 5-km resolution historical 2020 simulation and (b) yearly mean zonal moisture transport in the 25-km resolution historical 2020 simulation. Changes in yearly mean zonal moisture transport for the La Niña–like warming pattern simulations at (c) 5-km resolution and (d) 25-km resolution. Changes in yearly mean zonal moisture transport for the El Niño–like warming pattern simulations at (e) 5-km resolution and (f) 25-km resolution.

regions is dampened, inducing a negative moisture feedback on the circulation response (Figs. 20e,f).

Although, on daily mean time scales and relatively large spatial scales, it was not possible to detect a relationship between upper-level atmospheric temperature anomalies and rainfall over the western Pacific in the historical 2020 experiments (section 5a), in the La Niña–like warming pattern simulations, considerable upper-level temperature gradients are established across the tropical Pacific (Figs. 21c,d). This shows that the tropical atmosphere can sustain significant temperature gradients in the upper troposphere generated by deep convection (Keil et al. 2023). This is a cautious tale with regard to the often used and cited weak temperature gradient approximation in the tropics. In both, the lower and upper troposphere temperature gradients in the tropics can be significant, and the tendency of the tropical atmosphere to

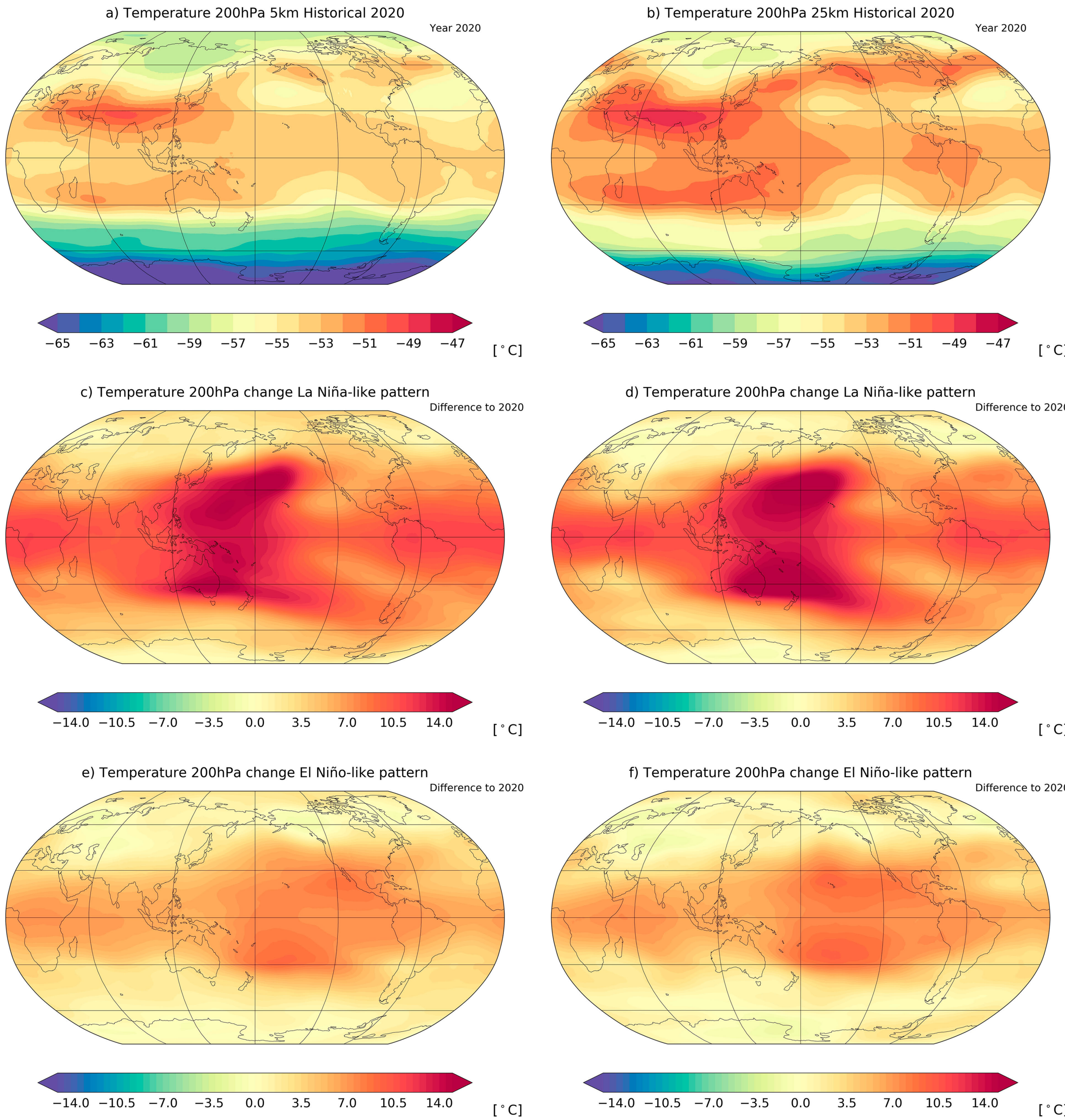

FIG. 21. (a) Yearly mean temperature at 200 hPa in the 5-km resolution historical 2020 simulation and (b) yearly mean temperature at 200 hPa in the 25-km resolution historical 2020 simulation. Changes in yearly mean temperature at 200 hPa for the La Niña–like warming pattern simulations at (c) 5-km resolution and (d) 25-km resolution. Changes in yearly mean temperature at 200 hPa for the El Niño–like warming pattern simulations at (e) 5-km resolution and (f) 25-km resolution.

equilibrate these gradients leads to large-scale circulations which include, but are not restricted to, divergent circulations (Sobel 2002).

6. Summary and conclusions

The present study aims to explore how clouds, convection, and the tropical circulation respond to different warming patterns. A main motivation is to better understand the observed variability and warming trends over the tropical Pacific in recent decades (L'Heureux et al. 2013; England et al. 2014; Tomassini 2020; Seager et al. 2022; Wills et al. 2022). It has been argued that low-resolution coupled climate models struggle to reproduce the historical evolution of the tropical Pacific SSTs. A main feature of the climate system over the tropical Pacific is the Walker circulation which connects the western Pacific deep convective regions with areas of subsidence in the eastern tropical Pacific. But also, gravity waves and convectively coupled tropical waves communicate temperature and moisture anomalies in the Pacific basin over large distances, ultimately a consequence of the fact that the tropical atmosphere cannot sustain larger temperature and pressure gradients in the midtroposphere due to the smallness of the Coriolis parameter near the equator. Thus, the interaction between moist convection and the tropical circulation likely plays an important role in shaping the particular response of the coupled atmosphere–ocean system to warming in the tropical Pacific region (Back and Bretherton 2005).

The role of clouds in influencing the sensitivity of the climate system to warming and the significance of the coupling between moist convection and the tropical circulation is explored in historical year 2020 simulations and two warming experiments in which two different SST patterns are added to the historical daily varying SSTs of the year 2020. Given that the resolution of the models that have been used to study climate change in the past is a potential concern, two sets of Met Office Unified Model simulations are examined. In one cutting-edge set of experiments, a global convection-permitting model at nominal 5-km resolution is used; in the second set of simulations, a 25-km resolution global model in which convection is parameterized is employed. This allows for assessing what effect explicitly resolving deep convection has on key mechanisms that govern the characteristics and magnitude of climate change, especially over the tropical Pacific. The 25-km resolution is still considerably finer than what is currently typically used in century-long integrations of global coupled climate models.

The important role of tropical Pacific SST patterns in determining the sensitivity of the climate system to warming is confirmed. Under a La Niña–like warming scenario, deep convection over the western Pacific is enhanced; the zonal circulation over the basin and the descending motion over the eastern Pacific are strengthened. Over the eastern Pacific, the atmospheric profiles become more stable, and a strong capping inversion is established in the lower troposphere. As a consequence, relatively more moisture is trapped in the boundary layer and low cloud cover, and therefore, albedo increases over the area leading to a negative shortwave cloud feedback which reduces climate sensitivity. A substantial upper-tropospheric east–west temperature gradient is established which promotes the stronger zonal flow and, as a result, stronger subsidence motion over the eastern Pacific.

The cloud changes over the eastern Pacific are not purely a local response; they are a consequence of the changing structure of the atmosphere across the tropics and related larger-scale circulation changes. This can be identified in the historical year 2020 simulations on daily time scales. Enhanced rainfall over the western Pacific is related to stronger 200-hPa zonal winds over the central Pacific and downward vertical motion in the midtroposphere over the eastern Pacific. Rainfall over the deep convective region is closely connected to low-level and upper-tropospheric divergence and lower-tropospheric moist static energy anomalies. The dynamics and variability of moisture appear to play an active role in governing these moist static energy anomalies: low-level advection of moisture from the east toward the Maritime Continent can be used as a predictor for temperature anomalies and rainfall over the western Pacific several days ahead. In contrast, no significant connection of rainfall with surface latent heat fluxes or radiative flux variability was detected on daily time scales. The relations in the historical experiments are consistent with the response seen in the warming pattern simulations. Increased westward zonal moisture advection in the La Niña–like warming scenario is related to enhanced deep convection in the western Pacific, a stronger zonal circulation, and stronger subsidence in the eastern Pacific. However, most of the changes in the zonal circulation over the tropical Pacific are not attributable to the divergent but the rotational component of the zonal wind. Although the rainfall and related upper-level divergence are more strongly connected with the divergent zonal wind in the historical year 2020 simulation on daily time scales, the changes in the nondivergent zonal wind are an important aspect in the response as seen in the La Niña–like warming experiment.

Evidence is presented for the important role of a positive moisture–convection–circulation feedback in driving ENSO-like dynamics over the tropical Pacific. This is reminiscent of the "thermally coupled Walker circulation" mechanism proposed by Clement et al. (2011) which does not depend on ocean heat transport. Based on the analysis of slab ocean simulations, Clement et al. (2011) suggested a wind–evaporation–surface temperature feedback and a role of cloud shortwave radiative effects in producing ENSO-like variability. In the present study, we were not able to identify a significant influence of latent heat fluxes or radiative effects on time scales of days but uncovered evidence for an active role of moisture advection and convective activity in initiating larger-scale zonal circulations over the tropical Pacific region which are particularly relevant when interpreting the La Niña–like warming simulation [see Inoue et al. (2021) for a more general discussion of the important role of horizontal moisture advection for rainfall variability over tropical oceans]. A similar perspective on the active role of moisture in tropical dynamics and variability was suggested by Sobel (2002) using a theoretical framework of balanced equations based on the weak temperature gradient approximation.

The El Niño–like warming pattern is more uniform over the tropical oceans and more similar to the SST patterns that low-resolution global coupled climate models project in century-long climate integrations. It is therefore important to understand what the near-uniform SST warming implies in terms of cloud feedbacks and atmospheric circulation changes. Changes in larger-scale circulations, upper-tropospheric temperature gradients, and lower-tropospheric stability are muted compared to the La Niña–like warming experiment. Accordingly, the shape of the distributions of vertical motion in the tropics changes less distinctly, a feature that is closely related to the less pronounced increase in moisture and moist static energy in the convergence zones over the tropical oceans in the El Niño–like warming pattern simulation compared to the La Niña–like warming pattern experiment. The absolute magnitude of the local temperature change alone does not govern the response of the convective regimes, and the characteristics of the atmospheric circulation distributions, changes in temperature gradients, and resulting moisture dynamics are essential. Accordingly, negative cloud feedbacks in the eastern Pacific subsidence region are extenuated in the El Niño–like warming pattern simulation, an important aspect of global relevance in the context of climate projections.

The experiments discussed in the present study involve simulations that are shorter than what is usually considered in climate studies. Natural variability enters the methodological approach in different ways. Natural variability plays a role in the choice of the reference year, it affects the definition of the warming patterns, and the chosen initial conditions in the 1-yr-long simulations can influence the results. However, the signals from the distinct warming patterns are large compared to the impact of a particular choice of a reference year or specifically selected initial conditions. Moreover, as mentioned in the introduction, the definition of warming patterns involves natural variability, but the focus of the present work is not to filter out a hypothetical climate change signal or to quantify the uncertainty in possible future climates. What is important is that the processes discussed in the study, mainly aspects related to clouds and convection, take place on time scales that are typically shorter than 1 year. Given that the SSTs are prescribed, that includes the rearrangement of larger-scale circulations or changes in the vertical structure of the atmosphere over the tropical Pacific.

In the grand scheme of things, the differences between the convection-permitting 5-km resolution simulations and the parameterized convection 25-km resolution experiments presented here may seem somewhat unspectacular at first. It is probably fair to say that they are more subtle than expected. For instance, even though the coupling between convection and the circulation is typically stronger in convection-permitting models, the correlation between daily mean rainfall over the western Pacific deep convective region and the daily mean central Pacific 200-hPa zonal wind is somewhat more pronounced in the historical 25-km resolution simulation compared to the convection-permitting 5-km resolution experiment. This suggests that the convection scheme is able to create marked responses to low-level moist static energy anomalies on shorter time scales. However, when using 5-day integrated sums of rainfall to predict the 200-hPa zonal winds 5 days ahead, the correlation is found to be distinctly stronger in the 5-km resolution convection-permitting experiment. Thus, the spatial and temporal intermittency and fast reaction time scale of the convection scheme might compromise longer-term and larger-scale interactions between moist convection, clouds, and the atmospheric circulation. The differences in the cloud and atmospheric circulation response to the different warming patterns between the convection-permitting 5-km resolution simulations and the 25-km resolution parameterized convection experiments are moderate in the atmosphere-only experiments presented here, but they are significant enough to potentially have a considerable impact in fully coupled ocean–atmosphere climate simulations. The markedly stronger low-level easterly trade winds over the equatorial Pacific, and associated enhanced westward moisture transport, in the convection-permitting La Niña–like warming experiment compared to the corresponding parameterized convection simulation are of particular relevance in this context. It will be very interesting to test and further investigate this hypothesis in future research.

Acknowledgments. Constructive and insightful comments by three anonymous reviewers helped improve the manuscript and are gratefully acknowledged.

Data availability statement. The Unified Model simulations underlying this research are not publicly available due to the huge disk space required to store the data. The data can, however, be accessed through the JASMIN service of the U.K. Centre for Environmental Data Analysis (CEDA) upon request. All observational, reanalysis, and CMIP6 datasets used in this study are publicly available. ERA5 data (Hersbach et al. 2020) were downloaded from the Copernicus Climate Change Service (C3S) Climate Data Store (https://cds.climate.copernicus.eu/cdsapp#!/dataset/reanalysis-era5-pressure-levels). The GPM data (Huffman et al. 2019) were provided by the NASA Goddard Space Flight Center, which developed and computed the GPM IMERG dataset as a contribution to the GPM project, and archived at the NASA GES DISC (https://disc.sci.gsfc.nasa.gov/). The NOAA GlobalTemp version 5 dataset (Zhang et al. 2023) is available at https://www.ncei.noaa.gov/metadata/geoportal/rest/metadata/item/gov.noaa.ncdc:C01585/html. The HadCRUT5 dataset (Morice et al. 2021) is accessible via https://www.metoffice.gov.uk/hadobs/hadcrut5/, and the HadISST data (Rayner et al. 2003) can be downloaded from https://www.metoffice.gov.uk/hadobs/hadisst/data/download.html.

REFERENCES

Allan, R. P., K. P. Shine, A. Slingo, and J. A. Pamment, 1999: The dependence of clear-sky outgoing long-wave radiation on surface temperature and relative humidity. *Quart. J. Roy. Meteor. Soc.*, **125**, 2103–2126, https://doi.org/10.1002/qj.49712555809.

Andrews, T., J. M. Gregory, and M. J. Webb, 2015: The dependence of radiative forcing and feedback on evolving patterns of surface temperature change in climate models. *J. Climate*, **28**, 1630–1648, https://doi.org/10.1175/JCLI-D-14-00545.1.

——, and Coauthors, 2018: Accounting for changing temperature patterns increases historical estimates of climate sensitivity. *Geophys. Res. Lett.*, **45**, 8490–8499, https://doi.org/10.1029/2018GL078887.

——, and Coauthors, 2022: On the effect of historical SST patterns on radiative feedback. *J. Geophys. Res. Atmos.*, **127**, e2022JD036675, https://doi.org/10.1029/2022JD036675.

Armour, K. C., C. M. Bitz, and G. H. Roe, 2013: Time-varying climate sensitivity from regional feedbacks. *J. Climate*, **26**, 4518–4534, https://doi.org/10.1175/JCLI-D-12-00544.1.

Back, L. E., and C. S. Bretherton, 2005: The relationship between wind speed and precipitation in the Pacific ITCZ. *J. Climate*, **18**, 4317–4328, https://doi.org/10.1175/JCLI3519.1.

——, and ——, 2009: On the relationship between SST gradients, boundary layer winds, and convergence over the tropical oceans. *J. Climate*, **22**, 4182–4196, https://doi.org/10.1175/2009JCLI2392.1.

Bodas-Salcedo, A., J. P. Mulcahy, T. Andrews, K. D. Williams, M. A. Ringer, P. R. Field, and G. S. Elsaesser, 2019: Strong dependence of atmospheric feedbacks on mixed-phase microphysics and aerosol-cloud interactions in HadGEM3. *J. Adv. Model. Earth Syst.*, **11**, 1735–1758, https://doi.org/10.1029/2019MS001688.

Bolot, M., and Coauthors, 2023: Kilometer-scale global warming simulations and active sensors reveal changes in tropical deep convection. *npj Climate Atmos. Sci.*, **6**, 209, https://doi.org/10.1038/s41612-023-00525-w.

Bony, S., B. Stevens, D. Coppin, T. Becker, K. A. Reed, A. Voigt, and B. Medeiros, 2016: Thermodynamic control of anvil cloud amount. *Proc. Natl. Acad. Sci. USA*, **113**, 8927–8932, https://doi.org/10.1073/pnas.1601472113.

Boutle, I. A., J. E. J. Eyre, and A. P. Lock, 2014: Seamless stratocumulus simulation across the turbulent gray zone. *Mon. Wea. Rev.*, **142**, 1655–1668, https://doi.org/10.1175/MWR-D-13-00229.1.

Bretherton, C. S., M. E. Peters, and L. E. Back, 2004: Relationships between water vapor path and precipitation over tropical oceans. *J. Climate*, **17**, 1517–1528, https://doi.org/10.1175/1520-0442(2004)017<1517:RBWVPA>2.0.CO;2.

Cane, M. A., A. C. Clement, A. Kaplan, Y. Kushnir, D. Pozdnyakov, R. Seager, S. E. Zebiak, and R. Murtugudde, 1997: Twentieth-century sea surface temperature trends. *Science*, **275**, 957–960, https://doi.org/10.1126/science.275.5302.957.

Ceppi, P., and S. Fueglistaler, 2021: The El Niño–Southern Oscillation pattern effect. *Geophys. Res. Lett.*, **48**, e2021GL095261, https://doi.org/10.1029/2021GL095261.

Cheng, K.-Y., and Coauthors, 2022: Impact of warmer sea surface temperature on the global pattern of intense convection: Insights from a global storm resolving model. *Geophys. Res. Lett.*, **49**, e2022GL099796, https://doi.org/10.1029/2022GL099796.

Clement, A., P. DiNezio, and C. Deser, 2011: Rethinking the ocean's role in the Southern Oscillation. *J. Climate*, **24**, 4056–4072, https://doi.org/10.1175/2011JCLI3973.1.

DiNezio, P. N., A. C. Clement, G. A. Vecchi, B. J. Soden, B. P. Kirtman, and S.-K. Lee, 2009: Climate response of the equatorial Pacific to global warming. *J. Climate*, **22**, 4873–4892, https://doi.org/10.1175/2009JCLI2982.1.

Dong, Y., C. Proistosescu, K. C. Armour, and D. S. Battisti, 2019: Attributing historical and future evolution of radiative feedbacks to regional warming patterns using a Green's function approach: The preeminence of the western Pacific. *J. Climate*, **32**, 5471–5491, https://doi.org/10.1175/JCLI-D-18-0843.1.

Dübal, H.-R., and F. Vahrenholt, 2021: Radiative energy flux variation from 2001–2020. *Atmosphere*, **12**, 1297, https://doi.org/10.3390/atmos12101297.

England, M. H., and Coauthors, 2014: Recent intensification of wind-driven circulation in the Pacific and the ongoing warming hiatus. *Nat. Climate Change*, **4**, 222–227, https://doi.org/10.1038/nclimate2106.

Fueglistaler, S., 2019: Observational evidence for two modes of coupling between sea surface temperatures, tropospheric temperature profile, and shortwave cloud radiative effect in the tropics. *Geophys. Res. Lett.*, **46**, 9890–9898, https://doi.org/10.1029/2019GL083990.

——, and L. G. Silvers, 2021: The peculiar trajectory of global warming. *J. Geophys. Res. Atmos.*, **126**, e2020JD033629, https://doi.org/10.1029/2020JD033629.

Ghosh, R., and T. G. Shepherd, 2023: Storylines of Maritime Continent dry period precipitation changes under global warming. *Environ. Res. Lett.*, **18**, 034017, https://doi.org/10.1088/1748-9326/acb788.

Gross, M., and Coauthors, 2018: Physics–dynamics coupling in weather, climate, and Earth system models: Challenges and recent progress. *Mon. Wea. Rev.*, **146**, 3505–3544, https://doi.org/10.1175/MWR-D-17-0345.1.

Hartmann, D. L., B. D. Dygert, P. N. Blossey, Q. Fu, and A. B. Sokol, 2022: The vertical profile of radiative cooling and lapse rate in a warming climate. *J. Climate*, **35**, 6253–6265, https://doi.org/10.1175/JCLI-D-21-0861.1.

Held, I. M., and B. J. Soden, 2006: Robust responses of the hydrological cycle to global warming. *J. Climate*, **19**, 5686–5699, https://doi.org/10.1175/JCLI3990.1.

Hersbach, H., and Coauthors, 2020: The ERA5 global reanalysis. *Quart. J. Roy. Meteor. Soc.*, **146**, 1999–2049, https://doi.org/10.1002/qj.3803.

Hogikyan, A., L. Resplandy, and S. Fueglistaler, 2022: Cause of the intense tropics-wide tropospheric warming in response to El Niño. *J. Climate*, **35**, 2933–2944, https://doi.org/10.1175/JCLI-D-21-0728.1.

Holloway, C. E., S. J. Woolnough, and G. M. S. Lister, 2012: Precipitation distributions for explicit versus parametrized convection in a large-domain high-resolution tropical case study. *Quart. J. Roy. Meteor. Soc.*, **138**, 1692–1708, https://doi.org/10.1002/qj.1903.

Huffman, G. J., E. F. Stocker, D. T. Bolvin, E. J. Nelkin, and J. Tan, 2019: GPM IMERG final precipitation L3 half hourly 0.1 degree × 0.1 degree V06. Goddard Earth Sciences Data and Information Services Center (GES DISC), accessed 1 May 2023, https://doi.org/10.5067/GPM/IMERG/3B-HH/06.

Inoue, K., M. Biasutti, and A. M. Fridlind, 2021: Evidence that horizontal moisture advection regulates the ubiquitous amplification of rainfall variability over tropical oceans. *J. Atmos. Sci.*, **78**, 529–547, https://doi.org/10.1175/JAS-D-20-0201.1.

Jakob, C., and C. Schumacher, 2008: Precipitation and latent heating characteristics of the major tropical western Pacific cloud regimes. *J. Climate*, **21**, 4348–4364, https://doi.org/10.1175/2008JCLI2122.1.

Jeevanjee, N., 2022: Three rules for the decrease of tropical convection with global warming. *J. Adv. Model. Earth Syst.*, **14**, e2022MS003285, https://doi.org/10.1029/2022MS003285.

——, and S. Fueglistaler, 2020: On the cooling-to-space approximation. *J. Atmos. Sci.*, **77**, 465–478, https://doi.org/10.1175/JAS-D-18-0352.1.

Jenney, A. M., D. A. Randall, and M. D. Branson, 2020: Understanding the response of tropical ascent to warming using an energy balance framework. *J. Adv. Model. Earth Syst.*, **12**, e2020MS002056, https://doi.org/10.1029/2020MS002056.

Keil, P., H. Schmidt, B. Stevens, M. P. Byrne, H. Segura, and D. Putrasahan, 2023: Tropical tropospheric warming pattern explained by shifts in convective heating in the Matsuno–Gill model. *Quart. J. Roy. Meteor. Soc.*, **149**, 2678–2695, https://doi.org/10.1002/qj.4526.

L'Ecuyer, T. S., Y. Hang, A. V. Matus, and Z. Wang, 2019: Reassessing the effect of cloud type on Earth's energy balance in the age of active spaceborne observations. Part I: Top of Atmosphere and Surface. *J. Climate*, **32**, 6197–6217, https://doi.org/10.1175/JCLI-D-18-0753.1.

L'Heureux, M. L., S. Lee, and B. Lyon, 2013: Recent multidecadal strengthening of the Walker circulation across the tropical Pacific. *Nat. Climate Change*, **3**, 571–576, https://doi.org/10.1038/nclimate1840.

Lindzen, R. S., and S. Nigam, 1987: On the role of sea surface temperature gradients in forcing low-level winds and convergence in the tropics. *J. Atmos. Sci.*, **44**, 2418–2436, https://doi.org/10.1175/1520-0469(1987)044<2418:OTROSS>2.0.CO;2.

Loeb, N. G., W. Su, and S. Kato, 2016: Understanding climate feedbacks and sensitivity using observations of Earth's energy budget. *Curr. Climate Change Rep.*, **2**, 170–178, https://doi.org/10.1007/s40641-016-0047-5.

——, and Coauthors, 2018: Clouds and the Earth's Radiant Energy System (CERES) Energy Balanced and Filled (EBAF) top-of-atmosphere (TOA) Edition-4.0 data product. *J. Climate*, **31**, 895–918, https://doi.org/10.1175/JCLI-D-17-0208.1.

Luo, H., J. Quaas, and Y. Han, 2023: Examining cloud vertical structure and radiative effects from satellite retrievals and evaluation of CMIP6 scenarios. *Atmos. Chem. Phys.*, **23**, 8169–8186, https://doi.org/10.5194/acp-23-8169-2023.

Morice, C. P., and Coauthors, 2021: An updated assessment of near-surface temperature change from 1850: The HadCRUT5 data set. *J. Geophys. Res. Atmos.*, **126**, e2019JD03236, https://doi.org/10.1029/2019JD032361.

Myhre, G., E. J. Highwood, K. P. Shine, and F. Stordal, 1998: New estimates of radiative forcing due to well mixed greenhouse gases. *Geophys. Res. Lett.*, **25**, 2715–2718, https://doi.org/10.1029/98GL01908.

Neelin, J. D., and I. M. Held, 1987: Modeling tropical convergence based on the moist static energy budget. *Mon. Wea. Rev.*, **115**, 3–12, https://doi.org/10.1175/1520-0493(1987)115<0003:MTCBOT>2.0.CO;2.

——, O. Peters, and K. Hales, 2009: The transition to strong convection. *J. Atmos. Sci.*, **66**, 2367–2384, https://doi.org/10.1175/2009JAS2962.1.

Raymond, D. J., S. L. Sessions, A. H. Sobel, and Ž. Fuchs, 2009: The mechanics of gross moist stability. *J. Adv. Model. Earth Syst.*, **1**, 9, https://doi.org/10.3894/JAMES.2009.1.9.

Rayner, N. A., D. E. Parker, E. B. Horton, C. K. Folland, L. V. Alexander, D. P. Rowell, E. C. Kent, and A. Kaplan, 2003: Global analyses of sea surface temperature, sea ice, and night marine air temperature since the late nineteenth century. *J. Geophys. Res.*, **108**, 4407, https://doi.org/10.1029/2002JD002670.

Richards, B. D. G., D. D. B. Koll, and T. W. Cronin, 2021: Seasonal loops between local outgoing longwave radiation and surface temperature. *Geophys. Res. Lett.*, **48**, e2021GL092978, https://doi.org/10.1029/2021GL092978.

Seager, R., M. Cane, N. Henderson, D.-E. Lee, R. Abernathey, and H. Zhang, 2019: Strengthening tropical Pacific zonal sea surface temperature gradient consistent with rising greenhouse gases. *Nat. Climate Change*, **9**, 517–522, https://doi.org/10.1038/s41558-019-0505-x.

——, N. Henderson, and M. Cane, 2022: Persistent discrepancies between observed and modeled trends in the tropical Pacific Ocean. *J. Climate*, **35**, 4571–4584, https://doi.org/10.1175/JCLI-D-21-0648.1.

Senior, C. A., and J. F. B. Mitchell, 2000: The time dependence of climate sensitivity. *Geophys. Res. Lett.*, **27**, 2685–2688, https://doi.org/10.1029/2000GL011373.

Shepherd, T. G., 2019: Storyline approach to the construction of regional climate change information. *Proc. Roy. Soc.*, **475A**, 20190013, https://doi.org/10.1098/rspa.2019.0013.

Sobel, A. H., 2002: Water vapor as an active scalar in tropical atmospheric dynamics. *Chaos*, **12**, 451–459, https://doi.org/10.1063/1.1480795.

——, 2007: Simple models of ensemble-averaged tropical precipitation and surface wind, given the sea surface temperature. *The Global Circulation of the Atmosphere*, T. Schneider and A. H. Sobel, Eds., Princeton University Press, 219–251.

Stevens, B., S. C. Sherwood, S. Bony, and M. J. Webb, 2016: Prospects for narrowing bounds on Earth's equilibrium climate sensitivity. *Earth's Future*, **4**, 512–522, https://doi.org/10.1002/2016EF000376.

Tomassini, L., 2020: The interaction between moist convection and the atmospheric circulation in the tropics. *Bull. Amer. Meteor. Soc.*, **101**, E1378–E1396, https://doi.org/10.1175/BAMS-D-19-0180.1.

——, and Coauthors, 2013: The respective roles of surface temperature driven feedbacks and tropospheric adjustment to CO_2 in CMIP5 transient climate simulations. *Climate Dyn.*, **41**, 3103–3126, https://doi.org/10.1007/s00382-013-1682-3.

——, A. Voigt, and B. Stevens, 2015: On the connection between tropical circulation, convective mixing, and climate sensitivity. *Quart. J. Roy. Meteor. Soc.*, **141**, 1404–1416, https://doi.org/10.1002/qj.2450.

——, and Coauthors, 2023: Confronting the convective gray zone in the global configuration of the Met Office Unified Model. *J. Adv. Model. Earth Syst.*, **15**, e2022MS003418, https://doi.org/10.1029/2022MS003418.

Tompkins, A. M., and F. Di Giuseppe, 2015: An interpretation of cloud overlap statistics. *J. Atmos. Sci.*, **72**, 2877–2889, https://doi.org/10.1175/JAS-D-14-0278.1.

Walters, D., and Coauthors, 2019: The Met Office Unified Model Global Atmosphere 7.0/7.1 and JULES Global Land 7.0 configurations. *Geosci. Model Dev.*, **12**, 1909–1963, https://doi.org/10.5194/gmd-12-1909-2019.

Watanabe, M., T. Iwakiri, Y. Dong, and S. M. Kang, 2023: Two competing drivers of the recent walker circulation trend. *Geophys. Res. Lett.*, **50**, e2023GL105332, https://doi.org/10.1029/2023GL105332.

Wilks, D. S., 2011: *Statistical Methods in the Atmospheric Sciences*. 3rd ed. Elsevier, 676 pp.

Wills, R. C. J., Y. Dong, C. Proistosecu, K. C. Armour, and D. S. Battisti, 2022: Systematic climate model biases in the large-scale patterns of recent sea-surface temperature and sea-level pressure change. *Geophys. Res. Lett.*, **49**, e2022GL100011, https://doi.org/10.1029/2022GL100011.

Wing, A. A., and Coauthors, 2020: Clouds and convective self-aggregation in a multimodel ensemble of radiative-convective equilibrium simulations. *J. Adv. Model. Earth Syst.*, **12**, e2020MS002138, https://doi.org/10.1029/2020MS002138.

Zhang, H.-M., B. Huang, J. H. Lawrimore, M. J. Menne, and T. M. Smith, 2023: NOAA global surface temperature dataset (NOAAGlobalTemp), version 5. NOAA National Centers for Environmental Information, accessed 1 September 2024, https://doi.org/10.25921/9qth-2p70.

Zhang, Y., and S. Fueglistaler, 2020: How tropical convection couples high moist static energy over land and ocean. *Geophys. Res. Lett.*, **47**, e2019GL086387, https://doi.org/10.1029/2019GL086387.